# Variability of the Axial Morphology and of the Gravity Structure along the Central Spreading Ridge (North Fiji Basin): Evidence for Contrasting Thermal Regimes

EULÀLIA GRÀCIA[1,2], CHANTAL TISSEAU[1], MÁRCIA MAIA[1], THIERRY TONNERRE[1], JEAN-MARIE AUZENDE[3]* and YVES LAGABRIELLE[1]

[1] *CNRS-URA 1278 Domaines Océaniques, Université de Bretagne Occidentale, 6 Av. Le Gorgeu, BP 452, 29275 Brest, France*
[2] *UA Geociències Marines CSIC-UB, GRQ Geociències Marines, Dpt. de Geologia Dinàmica, Geofísica i Paleontologia, Universitat de Barcelona, 08028 Barcelona, Spain*
[3] *DRO/GM, IFREMER-Centre de Brest, BP 70, 29280 Plouzané, France*
* *Now at: Dpt. Géologie-Géophysique, Centre ORSTOM, BP A5, Nouméa, Nouvelle Calédonie*

(Received 3 February 1995; accepted 17 August 1995)

**Key words:** Back-arc basin, spreading center, axial morphology, Mantle Bouguer Anomaly, segmentation, thermal modelling

**Abstract.** The Central Spreading Ridge (CSR) is located in the central part of the North Fiji Basin, a complex back-arc basin created 12 Ma ago between the Pacific and Indo-Australian plates. The 3.5 Ma old CSR is the best developed, for both structure and magmatism, of all the spreading centers identified in the basin, and may be one of the largest spreading systems of the west Pacific back-arc basins. It is more than 800 km long and 50–60 km wide, and has been intensively explored during the French-Japanese STARMER project (1987–1991).

The CSR is segmented into three first order segments named, from north to south, N160°, N15° and N–S according to their orientation. This segmentation pattern is similar to that found at mid-ocean ridges. The calculated spreading rate is intermediate and ranges from 83 mm/yr at 20°30′ S to 50 mm/yr at 17° S. In addition, there is a change in the axial ridge morphology and gravity structure between the northern and southern sections of the CSR. The axial morphology changes from a deep rift valley (N160° segment), to a dome split by an axial graben (N15° segment) and to a rectangular flat top high (N–S segment). The Mantle Bouguer Anomalies obtained on the northern part of the CSR (N160°/N15° segments) show "bull's eye" structures associated with mantle upwelling at the 16°50′ S triple junction and also in the middle of the segments. The Mantle Bouguer Anomalies of the southern part of the ridge (N–S segment) are more homogeneous and consistent with the observed smooth topography associated with axial isostatic compensation.

At these intermediate spreading rates the contrast in bathymetry and gravity structure between the segments may reflect differences in heat supply. We suggest that the N160° and N15° segments are "cold" with respect to the "hot" N–S segment. We use a non-steady-state thermal model to test this hypothesis. In this model, the accretion is simulated as a nearly steady-state seafloor spreading upon which are superimposed periodic thermal inputs. With the measured spreading rate of 50 mm/yr, a cooling cycle of 200,000 yr develops a thermal state that permits to explain the axial morphology and gravity structure observed on the N160° segment. A spreading rate of 83 mm/yr and a cooling cycle of 120,000 yr would generate the optimal thermal structure to explain the characteristics of the N–S segment. The boundaries between the "hot" N–S segment and its "cold" bounding segments are the 18°10′ S and 20°30′ S propagating rifts. A heat propagation event along the N–S segment at the expense of the adjacent colder failing segments, can explain the sharp changes in the observed morphology and structure between the segments.

## Introduction

It has been observed that there is a strong dependence of axial morphology on the spreading rate (e.g. Menard, 1967; Macdonald, 1982). An axial depression is characteristic of slow spreading rates (less than 50 mm/yr), whereas an almost flat profile and a topographic high are systematically observed at intermediate (50–90 mm/yr) and fast (greater than 90 mm/yr) spreading rates (Macdonald, 1982; 1986). Exceptions to this general trend are noticed in ridges near hot-spots where axial highs are found at slow-spreading rates (e.g. Reykjanes Ridge, Laughton *et al.*, 1979). In other areas, where a fast spreading ridge contacts an old and cold lithosphere, a deep axial valley develops (Malinverno, 1993) (e.g. Pito Rift, Martinez *et al.*, 1991).

Axial valleys are considered dynamically stable features (Atwater and Mudie, 1973; Macdonald, 1982), and several steady-state models have been proposed to explain their presence at slow-spreading centers (Sleep, 1969; Lachenbruch, 1973; Anderson and Noltimier, 1973; Tapponnier and Francheteau, 1978; Phipps Morgan *et al.*, 1987; Chen and Morgan, 1990b). Recent multibeam bathymetry surveys around the world reveal a wide variety of ridge morphologic features at slow and intermediate rates instead of an ubiquitous axial depression. Changes from a volcanic dome to a rift

*Marine Geophysical Researches* **18:** 249–273, 1996.

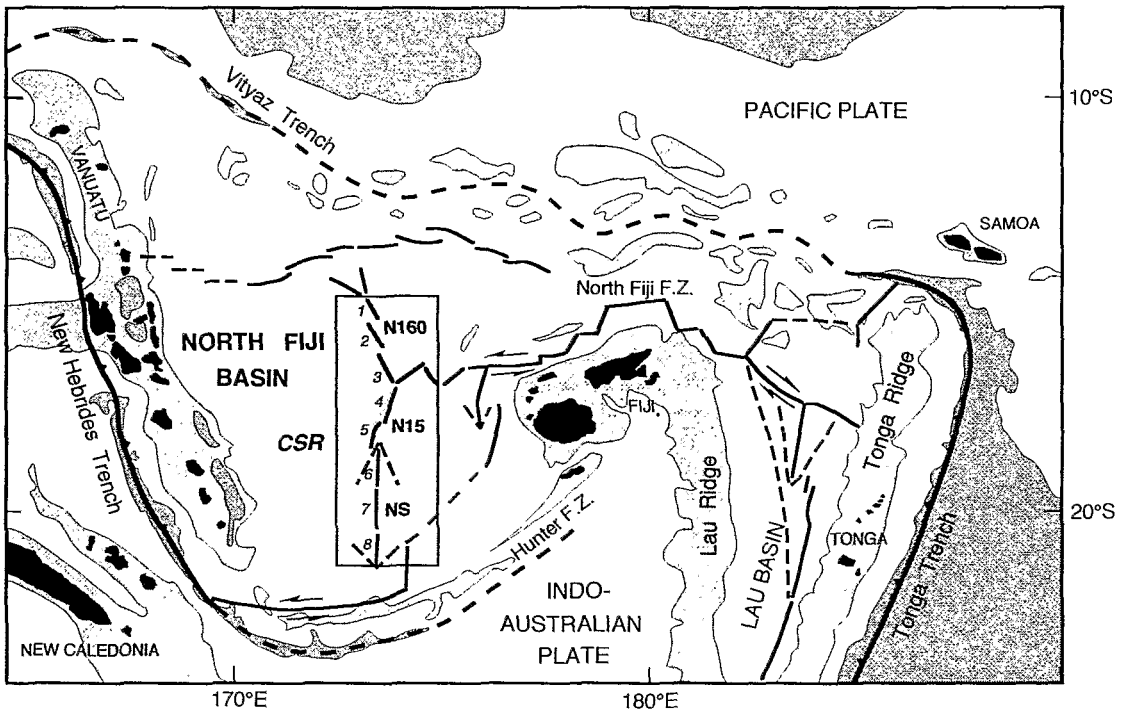


Fig. 1. Location of the Central Spreading Ridge (rectangle) in the North Fiji Basin. Thick lines mark the position of the present-day spreading axis and fracture zones. Tectonic elements of the northern part of the North Fiji and Lau Basins are taken from Parson *et al.* (1992), Pelletier *et al.* (1993), and Lagabrielle *et al.* (1994).

valley have been proposed from a segment of the Juan de Fuca Ridge (Kappel and Ryan, 1986), morphologic variations ranging from a deep median valley to a rifted axial dome, are observed at the Mid-Atlantic Ridge between 31° S and 34°30′ S (Fox *et al.*, 1991), and a contrast between an axial high and a marked rift at a constant intermediate spreading rate have been pointed out along the Australian-Antarctic Discordance (Palmer *et al.*, 1993) and the Pacific-Antarctic Ridge (Marks and Stock, 1994). This morphological variability suggests that, in addition to spreading rate, other parameters such as magma supply and/or crustal thickness exert a morphological control.

The Central Spreading Ridge (CSR) of the North Fiji Basin (southwest Pacific) is a mature back-arc spreading center which shows different axial morphologies with an intermediate spreading rate. In this paper we attempt to relate along-axis variations in morphology and gravity structure to different thermal regimes. We have compiled the available swath-bathymetry and gravity data and we use the Mantle Bouguer Anomaly to constrain our thermal models. A non-steady-state thermal model is used to explain the observed variations.

## 2. Geological Setting

The North Fiji Basin is a complex marginal basin created 12 Ma ago at the boundary of the Pacific and Indo-Australian plates (Pelletier *et al.*, 1993), between two subduction zones of opposite polarity: the New Hebrides and the Tonga-Kermadec trenches (Figure 1). Several extensional structures and spreading centers have been identified within the North Fiji Basin. The CSR appears to be the most evolved of the spreading zones (Auzende *et al.*, 1988a, b, 1990, 1991).

The basalts accreted along the CSR are predominantly MORB-type, although there is a geochemical back-arc signature on the northern and southern parts of the spreading center (Eissen, 1991, 1994; Lagabrielle *et al.*, 1994). Magnetic anomalies indicate that seafloor spreading began at the central part of the ridge about 3 Ma ago. More recently, about 1.5 Ma ago, changes in

Fig. 2. Bathymetric map (200 m contour interval) of the Central Spreading Ridge. The three first order segments (N 160°, N 15°, and N S) and the 16°50′ S triple junction are distinguished.

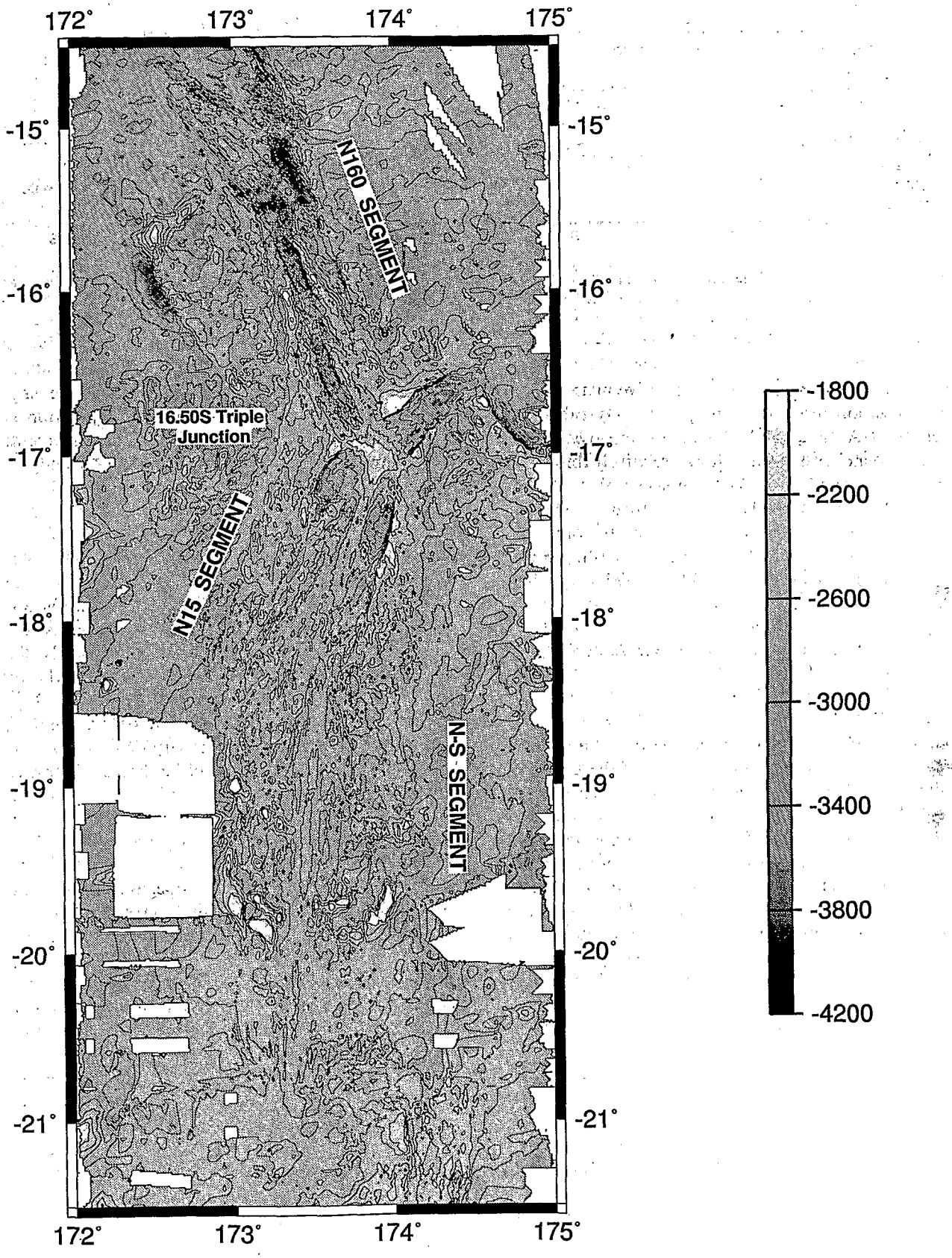
172°
173°
174°
175°
-15°
-16°
-17°
-18°
-19°
-20°
-21°
N160 SEGMENT
16.50S Triple Junction
N15 SEGMENT
N-S SEGMENT
-1800
-2200
-2600
-3000
-3400
-3800
-4200

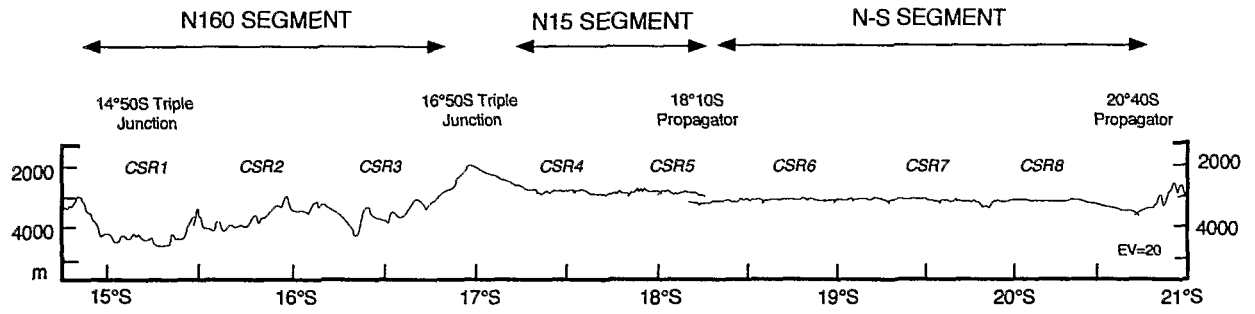


Fig. 3. Axial depth profile of the Central Spreading Ridge between 14°50′ S and 21° S. Note the rough axial topography and the small order segmentation of the N160° segment (CSR1 to CSR3) in comparison with the southern segments (CSR4 to CSR8).

the geodynamic setting and a successive plate-motion reorganization resulted in the present-day ridge segmentation (Auzende *et al.*, 1988a; Huchon *et al.*, 1994). Multi-channel seismic data show a relatively thin crust, with no evidence for an axial magma chamber reflector (Kisimoto *et al.*, 1994). There is extensive low-temperature hydrothermal activity, in addition to some sites of vigorously active high-temperature venting along the CSR (Auzende *et al.*, 1990, 1991; Bendel *et al.*, 1993).

## 3. Morphostructure of the Central Spreading Ridge

### 3.1. Previous works

Detailed bathymetric studies have revealed a suite of discontinuities that segment the axis of the CSR, including overlapping spreading centers, propagating rifts, offsets and *devals*, analogous to those described along mid-ocean ridges (Hey *et al.*, 1980; Macdonald and Fox, 1983; Macdonald *et al.*, 1991; Schouten *et al.*, 1985; Whitehead *et al.*, 1984). The fundamental difference between mid-ocean ridges and the CSR is the lack of major transform faults along the latter. This might be a general feature characterizing back-arc accretion, as is pointed out for the Woodlark Basin spreading center (Taylor *et al.*, 1995) or the South Pandora Ridge in the northern North Fiji Basin (Lagabrielle *et al.*, 1994).

The CSR axis extends 800 km, is 8–10 km wide, and trends roughly N–S changing in direction to the N160° E and N15° E, north and south of 16°50′ S, respectively. The axial depth ranges between 4400 m and less than 2000 m, reaching the shallowest point (1800 m) also at 16°50′ S. Three main segments, N160°, N15° and N–S (Figure 2) are observed along the CSR (Auzende *et al.*, 1988a, 1990; Huchon *et al.*, 1994; Tanahashi *et al.*, 1994).

Four main discontinuities bound the three segments (Figures 1, 2). The 14°50′ S triple junction is located at the northern tip of the N160° segment, where three grabens seem to converge (Auzende *et al.*, 1994). The 16°50′ S triple junction is located at the intersection between the N160° and N15° segments and the North Fiji Fracture Zone (Lafoy *et al.*, 1990; Jarvis and Kroenke, 1993). The 18°10′ S propagating rift occurs at the northern tip of the N–S segment where a clear V-shape structure is observed. The N15° failing rift retreats progressively whereas the N–S segment propagates northwards (De Alteriis *et al.*, 1993; Ruellan *et al.*, 1994). De Alteriis *et al.* (1993) and Tanahashi *et al.* (1994) also suggested that the N–S segment could be propagating southwards at 20°40′ S. The gravity data we present here confirm this idea, and will be discussed further on (see section 4).

### 3.2. Ridge segmentation

Three parameters can characterize segmentation along spreading ridges: the length of the segment, the longevity of the segment, and the offset separating the segments (Macdonald *et al.*, 1991). Along the whole CSR, neither the longevity nor the offset can be considered due to the youthfulness of the spreading center and the lack of large offsets and transforms. Thus, the length of the segment is the only parameter we measured in order to characterize the CSR segmentation.

The axial depth profile (Figure 3) shows a long-wavelength (150–250 km long) bathymetric pattern between the first-order segments (N160°, N15° and N–S) separated by first-order discontinuities (14°50′ S and 16°50′ S triple junctions, and 18°10′ S and 20°40′ S propagating rifts). Superimposed on this long-wavelength segmentation is a shorter-wavelength (50–90 km) segmentation caused by second-order discontinuities.

These smaller segments have been labelled from north to south, CSR1–CSR8.

3.2.1. *N160° First-Order Segment*

The N160° segment extends 210 km, between the 14°50′ S and the 16°50′ S triple junctions (Figure 4a). It is composed of three second-order segments (CSR1 to CSR3) which are a succession of long *en échelon* grabens (Figure 5a). Segment CSR1 is 63 km long, between 7.5 km and 15 km wide and reaches a depth of 4200 m. Segment CSR2 is offset 20 km to the east of segment CSR1 at 15°30′ S. Segment CSR2 is 82.5 km long, 12 km wide, and 3700 m deep. A 5 km right-lateral offset separates CSR2 and CSR3 at 16°15′ S. Segment CSR3 is 78 km long, 10.5 km wide, and 3600 m deep (Figures 4a, 5a).

Segments CSR2 and CSR3 are bound by two volcanic constructions, 135 km long and 2100 m high that become progressively wider southwards, reaching a width of 40 km near the 16°50′ S triple junction. These ridges connect with the axial valley trough a wall 1000 m high formed from several steps of inward facing scarps which would appear to be normal faults.

3.2.2. *N15° First-Order Segment*

The N15° segment extends from the 16°50′ S triple junction to 18°10′ S, and has a length of 165 km. It comprises the two second-order segments CSR4 and CSR5, separated by 17°50′ S offset. Segment CSR4 is 97 km-long, and is characterized by a 500 m high and 10.5 km wide axial ridge with a small axial graben 1.5–3 km wide.

The axial zone is bound by two curved grabens, 60 km wide and 3500 m deep. Such grabens might be relict structures related to the functioning of the 16°50′ S triple junction. CSR5 is 72 km long and characterized by a 3 km wide and 300 m high dome bordered by two elongated, curved depressions. The axis of segment CSR5 also shows a curved shape from 17°56′ S to 18°34′ S and overlaps with the northern portion of the N–S segment. Off-axis areas display a series of small-scale highs and lows that also trend N15° (Figures 4a, 5a).

3.2.3. *N–S First-Order Segment*

This segment extends from 18°10′ S to 21°45′ S and is 255 km long. Three second-order segments can be distinguished. Segment CSR6 is characterized by a dome 67.5 km long, 9 km wide and 100 m high. A small offset at 19°05′ S separates this segment from CSR7. A 71 km long dome, with the shallowest depth (2000 m) and the widest section (12 km) can be observed along the middle segment (CSR7). A small overlapping spreading center at 19°50′ S separates CSR7 and CSR8. This last segment is characterized by a 75 km long, 7.5 km wide and 100 m high axial dome. CSR6 propagates northwards whereas CSR8 seems to propagate southwards, as is suggested by the V-shaped pseudofaults (Figures 4b, 5b).

An important feature of the off-axis topography is the existence of volcanic cones and seamount chains. The volcanic cones are located between 19° S and 20° S, off-axis of the central part of segment CSR7 (Figures 4b, 5b). We have identified a total of ten symmetrical seamount chains, labelled A to E for the west flank and A′ to E′ for the eastern flank. These seamount chains exhibit conical volcanic edifices and ridges forming V-shaped alignments slightly asymmetric with respect to the axis (Figure 5b). The average size of these volcanoes ranges from a basal diameter of 4–5 km up to 10–15 km. They rise above the abyssal plain by 500 up to 1300 m. Some of them show depressions up to 1–2 km in diameter that are interpreted as caldera collapses, suggesting magmatic chambers underneath (Batiza and Vanko, 1983). The trends of the chains are perpendicular to oblique (N 30°) with respect to the axis direction. Most seamounts are located within 25 km of the ridge axis and may be associated with the upwelling system beneath the ridge, although a mini-hotspot hypothesis (Shen *et al.*, 1993) has been put forward for the formation of the seamounts B and B′, 61 and 92 km off-axis respectively. The small isolated volcanic cones appear scattered over the basin floor. They have a basal diameter about 5 times smaller (1.5 km in average) than the seamount chains described above.

3.3. Seafloor tectonic fabric

The shaded relief maps derived from the swath-bathymetry (Figure 4) reveal high angle-slopes that parallel the ridge axis, and are interpreted as being the expression of faults. The topographic roughness seems to decrease towards the south from the N160° to the N–S segment, and the orientation of the fault pattern off-axis seems to mimic the present-day orientation of the ridge axis. It also clearly shows the dome-shaped topography along the N–S axis (Figure 4b).

The off-axis topography of the N160° and N15° first-order segments exhibits a series of topographic lows and highs with a periodicity of 200,000 yr assuming a spreading rate of 50 mm/yr (Figure 4a). The off-axis topography of the N–S segment is rather flat, except along pseudofaults of the north and south propagators where a series of topographic lows and highs occur every 120,000 yr (Figure 4b).

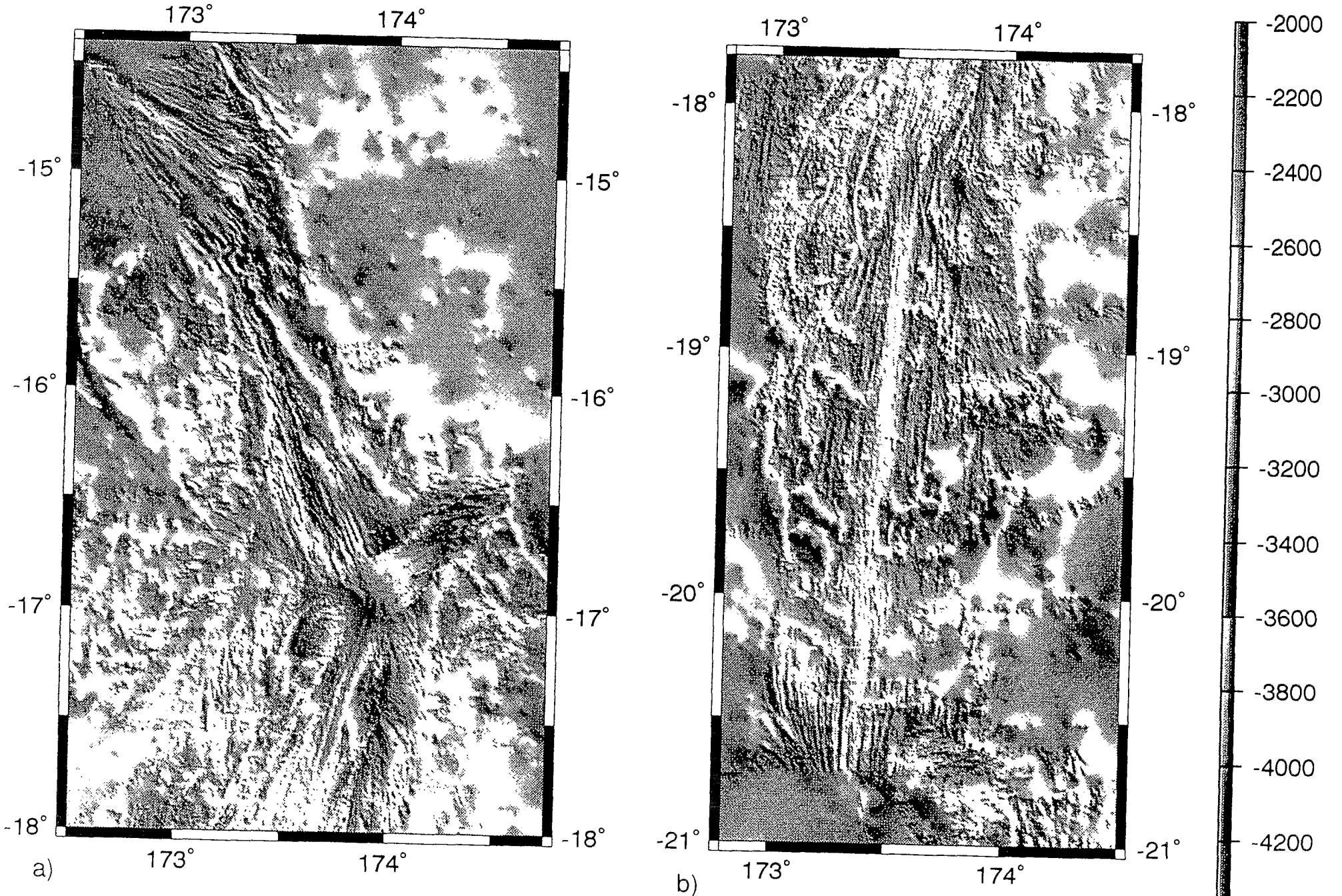


Fig. 4. Colour shaded relief map of a) northern and b) southern parts of the Central Spreading Ridge. These maps result from a compilation of the bathymetric data acquired during five cruises of the French-Japanese STARMER project (Kaiyo 87, 88, 89 and Yokosuka 90 and 91) and GEODAS database (NOAA/NGDC, 1992). Colour changes every 200 m. Illumination: N 45° E, elevation: 30°. The areas with detailed survey are shown by rough, small-scale topography, whereas zones where the bathymetry is interpolated are much smoother.

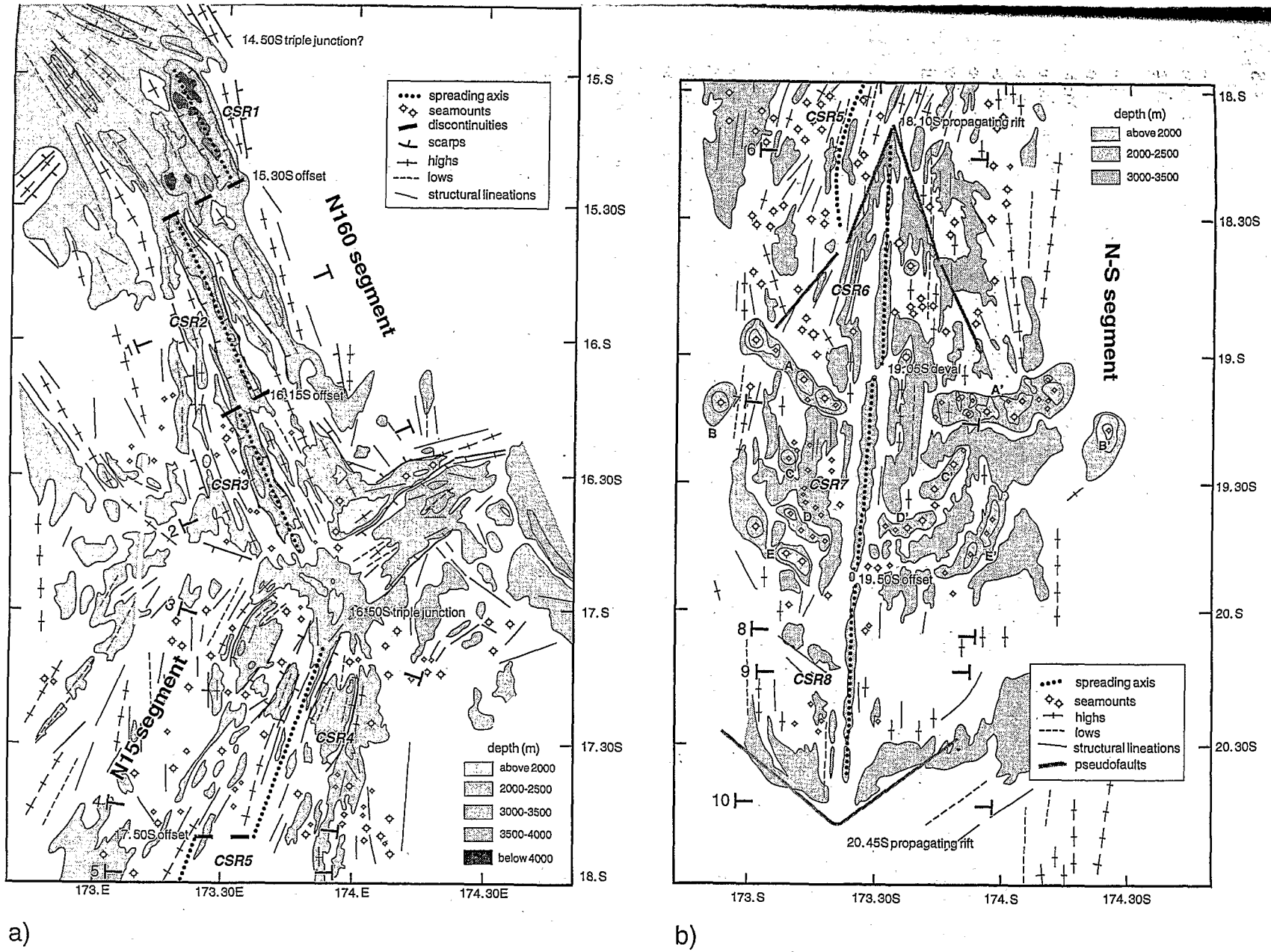


Fig. 5. Morphostructural interpretative maps of the Central Spreading Ridge between a) 15° S–18° S and b) 18° S–21° S. Note the ten seamount chains at both sides of the N-S axis labeled A–A′ to E–E′. Second-order segments and axial discontinuities are also indicated. Numbers 1 to 10 correspond to the location of the profiles depicted in Figures 12 and 13.

Inward facing faults seem to predominate on the N160° segment whereas both inward and outward faulting appear along the N-S segment, as has been suggested for slow and fast spreading ridges, respectively (Carbotte and Macdonald, 1990).

### 3.4. Axial morphology and spreading rate

A rift valley, on average 10 km wide and 1 km deep, runs along the crest of the N160° segment (Figure 6). Volcanism is very focused here and only present along the axial neovolcanic ridge (500 m wide and 200 m high), in the middle of the graben. Fault scarps, fissures and a thick sediment cover have been identified in submersible observations (Gràcia *et al.*, 1994). The axial morphology of the N160° segment is similar to those reported for slow-spreading ridges, such as the Mid-Atlantic Ridge (Macdonald, 1986; Purdy *et al.*, 1990; Grindlay *et al.*, 1992). The calculated spreading rate from the magnetic anomalies yield an intermediate value of 50 mm/yr (Huchon *et al.*, 1994) and an age of less than 1 Ma (Auzende *et al.*, 1991).

The axial morphology of the N15° segment is characterized by a double ridge (2000 m deep) split by a 2 km wide and 200 m deep axial graben (Figure 6). The most vigorous hydrothermal activity found along the CSR takes place in the inner part of the axial graben (Auzende *et al.*, 1990; Bendel *et al.*, 1993; Gràcia *et al.*, 1994). Magnetic anomalies suggest an age of 1 Ma for the N15° segment. The calculated spreading rate decreases from 66 mm/yr at 18° S to 52 mm/yr at 16°50′ S (Huchon *et al.*, 1994).

The N–S segment morphology is characterized by a central flat and rectangular axial rise locally cut by an axial summit caldera. A triangular shape is also observed in the middle of segment CSR7 (Figure 6). Both axial morphologies, rectangular and triangular, are typical of fast-spreading ridges, like the East Pacific Rise (Macdonald and Fox, 1988; Macdonald *et al.*, 1992). Along this segment, recent sheet-like lava flows erupted from fissures are found together with fossil hydrothermal activity (Bendel *et al.*, 1993; Gràcia *et al.*, 1994). Magnetic anomalies up to 2A (3.5 Ma) have been identified, and the spreading rate ranges from 83 mm/yr at 20°30′ S to 71 mm/yr at 19° S (Huchon *et al.*, 1994).

We have stacked across-axis bathymetric profiles, spaced every 10 minutes along-axis, for each of the three CSR segments identified (Figure 7). Segment N–S shows little variation in the axial morphology for distances less than 20 km off-axis. Segments N15° and N160° are much less homogeneous. For each of the segments, we have averaged all the strike profiles in an area ±20 km from the ridge axis (Figure 8). The N–S average cross section shows a smooth and flat profile. The N15° segment average section is represented by a dome split by an axial graben. A characteristic deep rift valley is found on the average profile corresponding to the N160° segment.

The morphologies observed along the CSR evolve from fast East Pacific Rise type (N–S segment), to intermediate (N15° segment), and to slow or Mid-Atlantic Ridge type (N160° segment). Despite these clear disparities, spreading rate decreases only from 83 to 50 mm/yr, and thus is of intermediate rate. Consequently, the morphological variations must be caused not only by spreading rate changes, but also by differences in the magmatic budget and thermal regime.

## 4. Gravity Structure of the Central Spreading Ridge

### 4.1. Gravity methods

We have compiled all the available shipborne gravity data for the area (NOAA/NGDC, 1992), comprising a total of 33,300 km, collected during numerous cruises and transits in this part of the North Fiji Basin. Due to the irregular quality of the data set, we performed a cross-over error analysis to check the consistency of the data between different cruises. Profiles that had no cross-over were checked visually, and some were rejected. In one case the Eötvos correction was entirely recalculated for the cruise, and good consistency with the remaining data was obtained. The whole data set were reduced to the same reference system (IGSN 71). Cross-over errors were computed and corrected for the data set using the algorithm of Hsu (1995). A track map of the selected cruises used in this study is presented in Figure 9.

To facilitate computation we separated the area in two sub-regions that overlap between latitudes 17°30′ S and 18°30′ S. These areas will be referred to hereafter as the northern and southern areas. The northern area has good gravity coverage, as shown in Figure 9, from the Kana Keoki 1982 and Moana Wave 1987 cruises of the Hawaii Institute of Geophysics (Kroenke *et al.*, 1990; Jarvis and Kroenke, 1993). For the southern area, CSR5 (N15° segment) and the whole N–S segment, the coverage is irregular, with sparse transit profiles, and only local full-coverage boxes (Figure 9), acquired during the Seapso 3 cruise (Auzende *et al.*, 1988a).

The central part of the southern area is particularly poorly covered, and anomalies with wavelengths

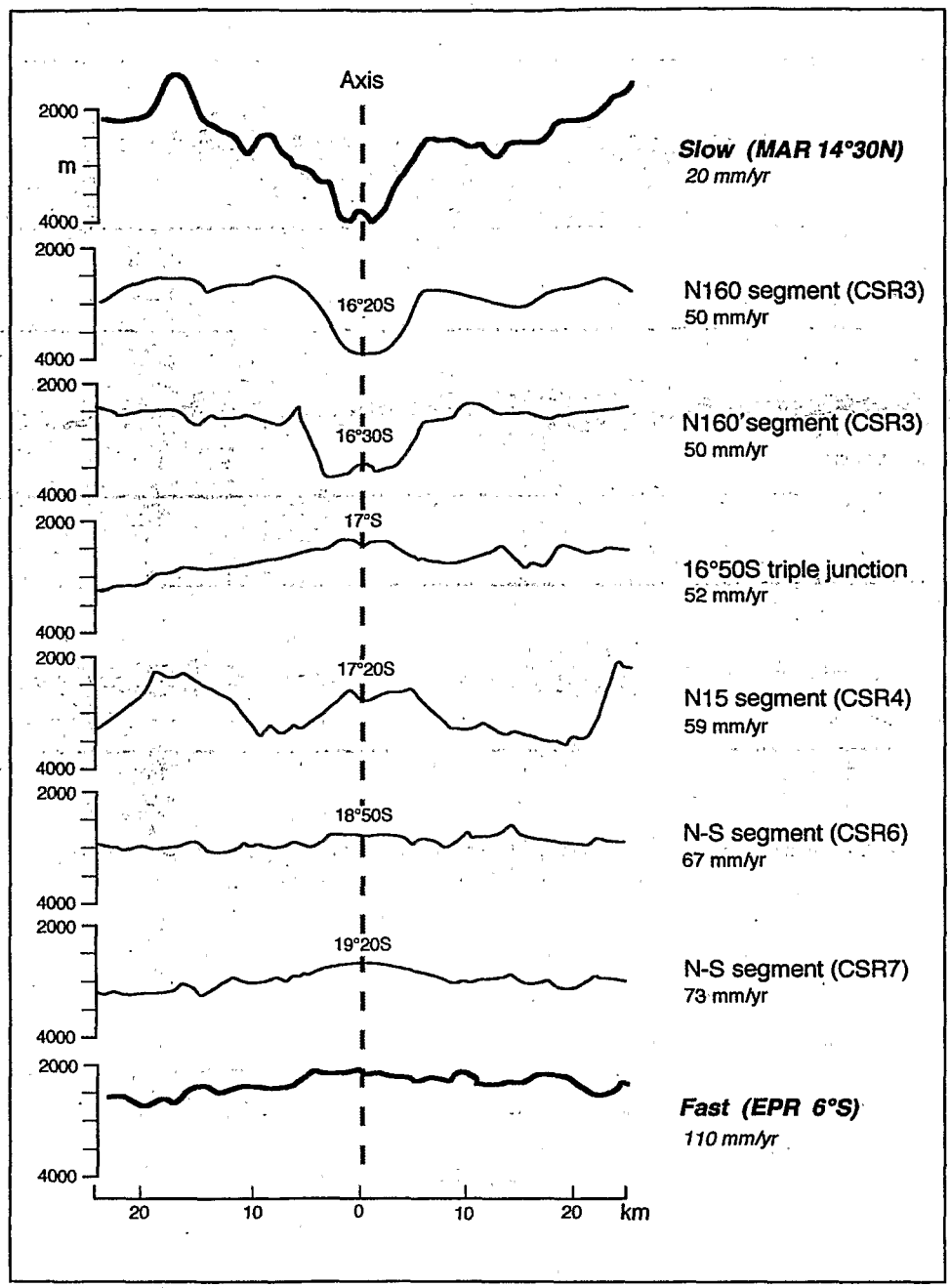


Fig. 6. Across-axis bathymetric profiles along the Central Spreading Ridge between 16°20′ S and 19°20′ S. Note the dramatic change in axial morphology between the different segments, while the whole spreading rate ranges between 50 to 73 mm/yr. Compare with the across axis profiles from the slow Mid-Atlantic Ridge and the Fast East Pacific Rise (Fox *et al.*, 1991). Vertical exaggeration is 5 to 1.

shorter than 80 km can not be resolved. In order to increase the spatial resolution in this central part we included free-air gravity anomalies derived from satellite altimetry (Sandwell and Smith, 1992). The spectral analysis of the free-air gravity computed from the satellite altimetry reveals that anomalies with wavelengths larger than 50 km can be correctly resolved. Although this value is larger that the 30 km found by Neumann *et al.* (1993) for the South Atlantic, where satellite coverage is denser, the use of the altimetric data still increases the quality of the compiled free-air gravity data in our area. Satellite data can be usefully em-

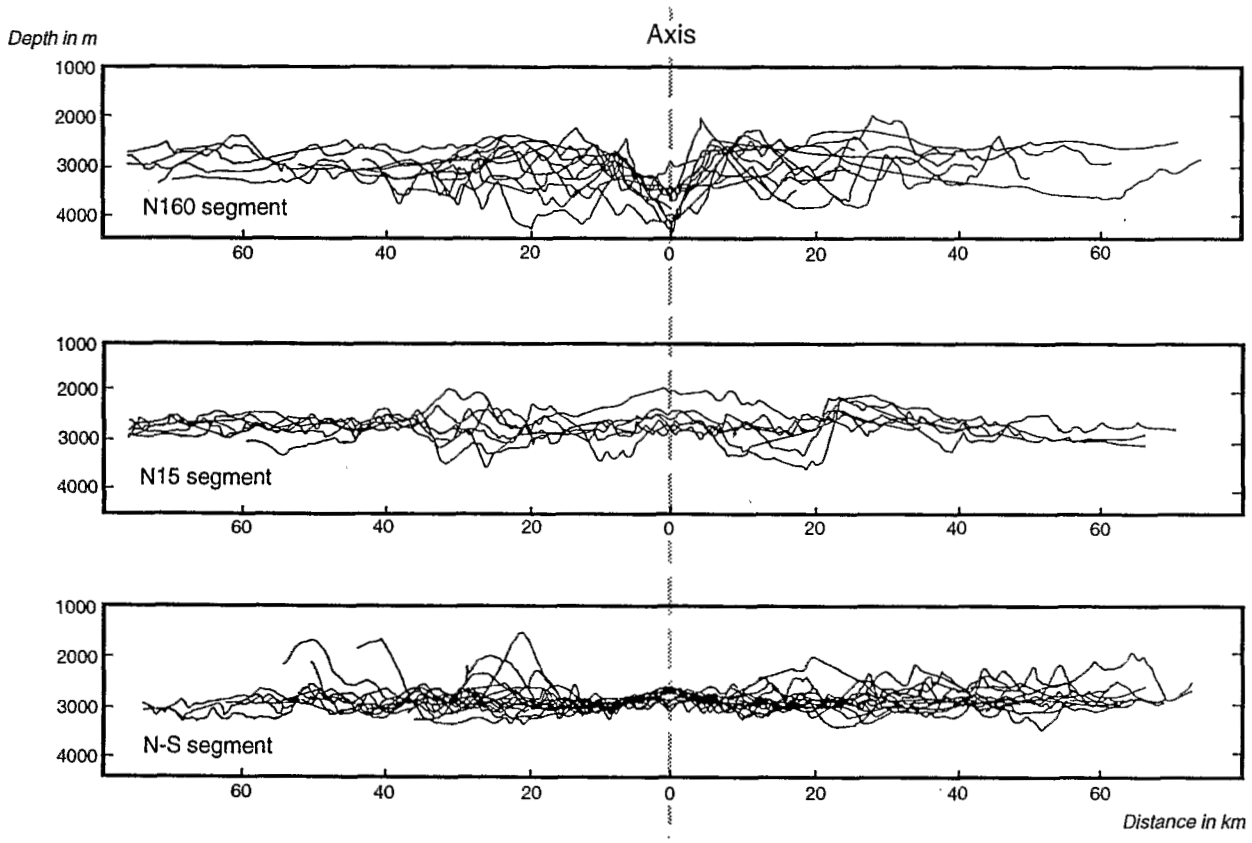


Fig. 7. Superposition of all the bathymetric cross-sections (spaced every 10') and separated by first-order segments. Note the homogeneity characterizing the axial domain of the N–S segment.

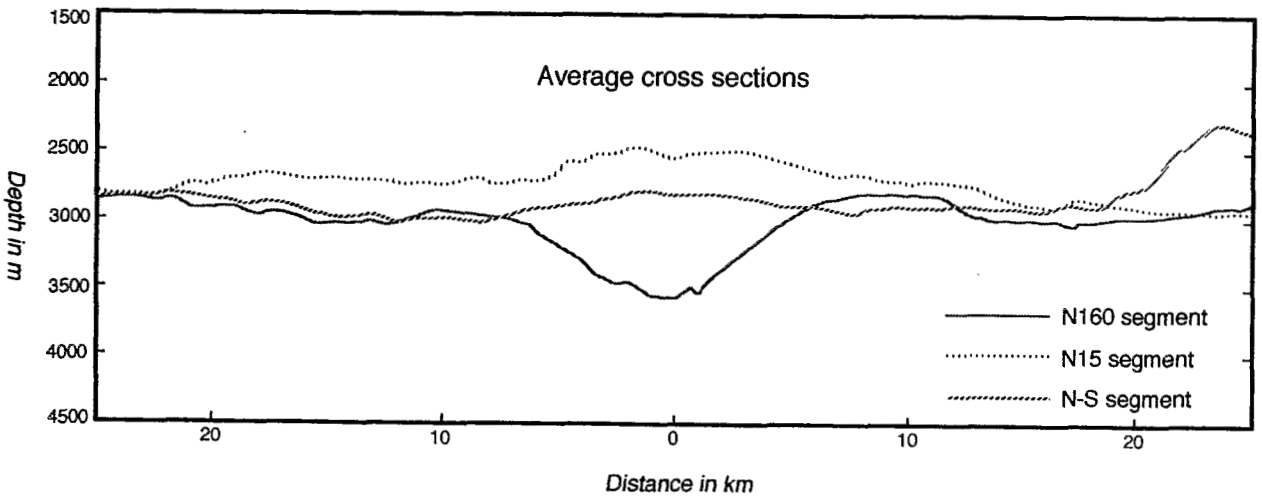


Fig. 8. Averaged cross-sections for each first-order segment.

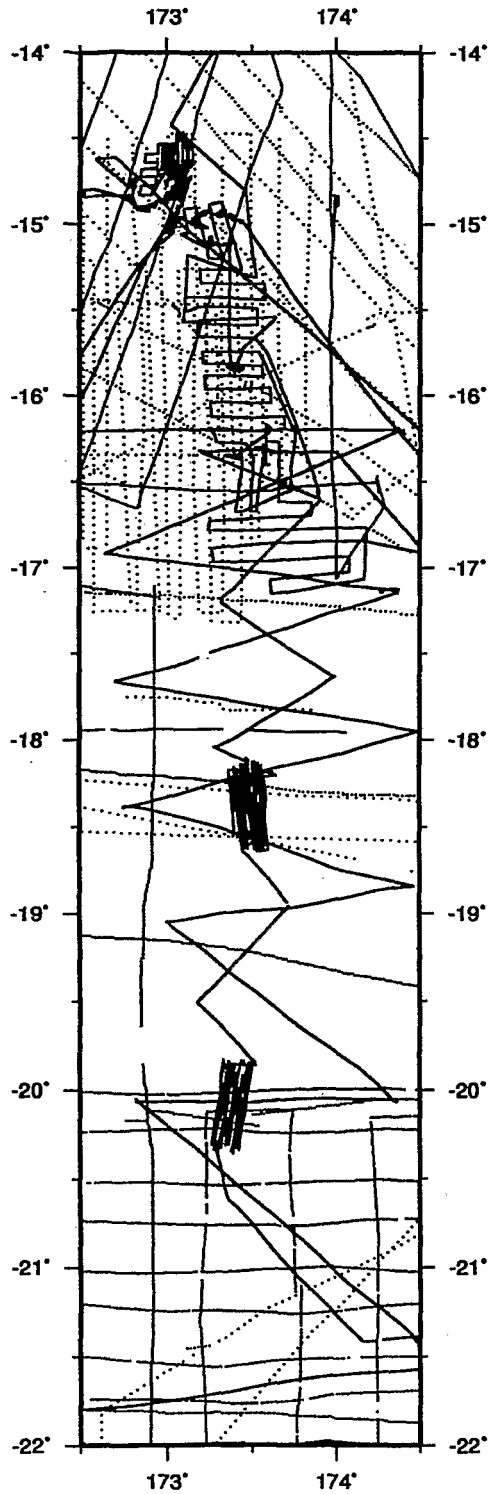


Fig. 9. Track map of the selected cruises for the gravity analysis of the Central Spreading Ridge (rectangle in Fig. 1). Note the good coverage for the northern part, whereas from 17°30′ S to the south the gravity coverage is poorer, with sparse profiles and some restricted full-coverage boxes.

ployed to help analysis where gaps are present, but shipborne data have always better quality. Thus, satellite-derived free-air gravity data were used only to fill some data gaps.

Free-air grids were obtained for both areas using the cubic B-spline approach (Inoue, 1986), and the Free-Air Anomaly (FAA) map obtained for the northern area with the full resolution of the data set is depicted in Figure 10a. In order to allow comparisons in a coherent way between the northern and southern areas, free-air grids were filtered to remove wavelengths shorter than 50 km (Figure 11a,b). The choice of the 50 km cut-off for the filter was determined by independent spectral analyses of both satellite and gridded marine data.

Mantle Bouguer Anomalies (MBA) were obtained using the classical approach developed by Prince and Forsyth (1988) and Kuo and Forsyth (1988) (Figures 10b, 11c,d). We computed the gravity effect of the water/crust and crust/mantle interfaces assuming a crustal thickness of 6 km. Crust and mantle densities were assumed to be uniform, 2.7 and 3.3 Mg/m$^3$ respectively, while water density was taken as 1.03 Mg/m$^3$. The gravity effects of the two interfaces were computed at each node of the grid with the FFT algorithm of Parker (1972). Model values were then sampled at each data point and then removed from the observed FAA. For the northern area, we present the resultant MBA without any filtering (Figure 10b). As for the free-air grid, the resultant MBA for the northern and southern areas was also filtered to remove wavelengths shorter than 50 km (Figure 11c,d). A comparison between Figures 10a, b and 11a, c shows that filtering preserves the main characteristics of the gravity field. In Figure 12 we show a comparison for three ship profiles between along track computed MBA (computed directly at each data point and unfiltered) and MBA values resampled along profile from the filtered merged grid. Both signals fit well for wavelengths longer than 50 km.

Due to the lack of good ages constraints, computation of residual MBA is not suitable. We will therefore restrain our analysis to a qualitative comparison of the variability of the MBA signal for the three segments.

### 4.2. Free-Air Anomalies

The FAA map of the northern part of the CSR between 14° S and 17°30′ S, comprising the N 160° segment and CSR4 (N 15° segment) is shown in Figure 10a. The FAA map is dominated by the effect of the water-crust interface and thus mimics the bathymetry (Figure 4a).

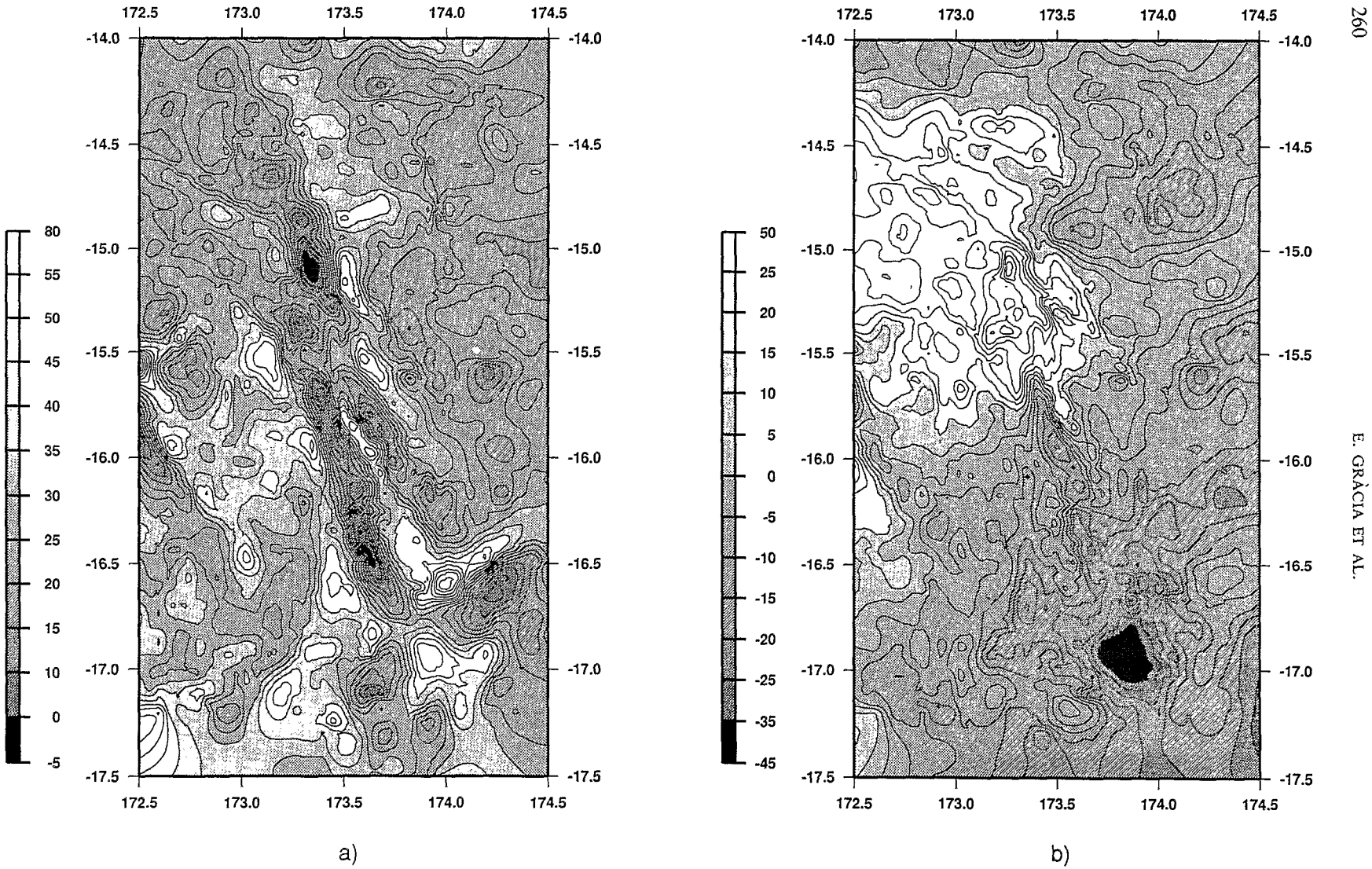


Fig. 10. a) Free-Air Anomaly map of the northern part of the Central Spreading Ridge. b) Mantle Bouguer Anomaly map of the northern part of the Central Spreading Ridge. These maps are created with the maximum resolution of the data.

The anomaly lows (–20 mGal) are associated with greater depths and rift valleys arranged *en échelon* along the N160° segment. Maximum positive anomalies (70 mGal) occur over topographic highs such as the 16°50′ S triple junction and the flanks of the CSR2, CSR3 and CSR4 segments (Figure 10a).

On the filtered FAA map of the northern part (Figure 11a), the main features are still recognizable. The FAA map of the southern part of the CSR (17°30′ S and 22° S), comprising the CSR5 (N15° segment) and the N–S segment is shown in Figure 11b. The N–S segment, is characterized by a small anomaly gradient (±10 mGal) consistent with its smooth axial topography. The off-axis seamounts are characterized by positive anomalies (more than 40 mGal).

### 4.3. Mantle Bouguer Anomalies

The MBA is related to the sub-seafloor density structure (Figures 10b, 11c,d) and reflects the gravity field arising from density anomalies in the crust or in the mantle. The interpretation of the MBA can be made in terms of crustal thickness and density variations, mantle density variations thermally induced, or by a combination of these mechanisms.

In the northern area (N160° segment) there is a strong negative signature (–50 mGal) passing from a "bull's-eye" (centered at the 16°50′ S triple junction) to an elongated shape (Figure 10b). Elongated anomalies (–25 mGal) appear also centered in the middle of segments CSR2 and CSR3, and may indicate the propagation of the CSR2 and CSR3 segments towards the north. The tip of the propagator is located at 15°50′ S, at the point where the two triangular ridges bordering the rift valley end (see Figure 10a). From this point to the north, at about 14°20′ S, the large positive anomaly observed (50 mGal) is possibly related to old and cold crust (Figure 10b).

On the downgraded MBA map of the northern CSR (Figure 11c) the main features described in Figure 10b are still recognizable. The MBA map of the southern part of the CSR (Figure 11d) shows a very uniform signature. As the bathymetric and structural maps indicate (Figures 4b, 5b), the N–S segment propagates north, towards the negative anomaly zone of the 16°50′ S triple junction. Between 20° S and 21° S there is a V-shaped structure, visible both in bathymetry and gravity. This structure is probably related to the southwards propagation of the N–S segment into a zone of old, cold crust with a very high positive gravity anomaly (55 mGal). The off-axis seamounts have a negative anomaly (–10 mGal) which may be related to a locally thickened crust.

MBA computed along ship tracks are represented in Figure 13 together with the corresponding bathymetric profiles. Profiles crossing the N15° and N160° segments show sharp variations in the MBA signal. In contrast, the signal on the N–S segment has a small variation (a few mGal) from one profile to the other and, like the bathymetry itself, is smooth and regular.

## 5. Discussion

### 5.1. Along-axis bathymetric and gravity variability

A synthesis of the main bathymetric, gravimetric, and petrologic results and observations along the CSR are presented in Table I. We can distinguish two different crustal domains, an old domain and a young domain. The old domain corresponds to crust created between 12 and 3.5 Ma (Pelletier *et al.*, 1993), before the initiation of oceanic spreading along the CSR. Its morphology is predominantly flat and uniform with an average depth of 3000 m. The MBA in these areas show strong positive anomalies between 20 to 55 mGal, that we interpret as corresponding to old cold crust. This area is mainly composed by BABB lavas with some traces of OIB (Eissen *et al.*, 1994) (Table Ia).

The young domain corresponds to oceanic crust created along the CSR since 3.5 Ma to the present-day. Two types of spreading center can be assumed based on their magmatic budget: a "cold"-type spreading center, which corresponds to the northern part of the CSR, and a "hot"-type for the southern part (Table Ib).

While maintaining an intermediate spreading rate (50–83 mm/yr), the CSR is characterized by an axial morphologic variability both spatially (along-strike) and temporally (across-strike). The "cold" spreading centers show an axial morphology characterized by a deep rift valley (N160° segment) or an axial graben (N15° segment), similar to those observed at the Mid-Atlantic Ridge. The roughness of the on- and off-axis topography is very pronounced. The morphology described above and the presence of an interrupted neovolcanic ridge indicates that magmatism is discontinuous along-axis (nonsteady-state) and restricted to this area, with no evidence for off-axis volcanic activity (Table Ib). In contrast, the "hot" spreading center represented by the N–S segment has an axial topography similar to that of the East Pacific Rise: a wide volcanic dome, locally with an axial summit caldera. The axial morphology together with the submersible

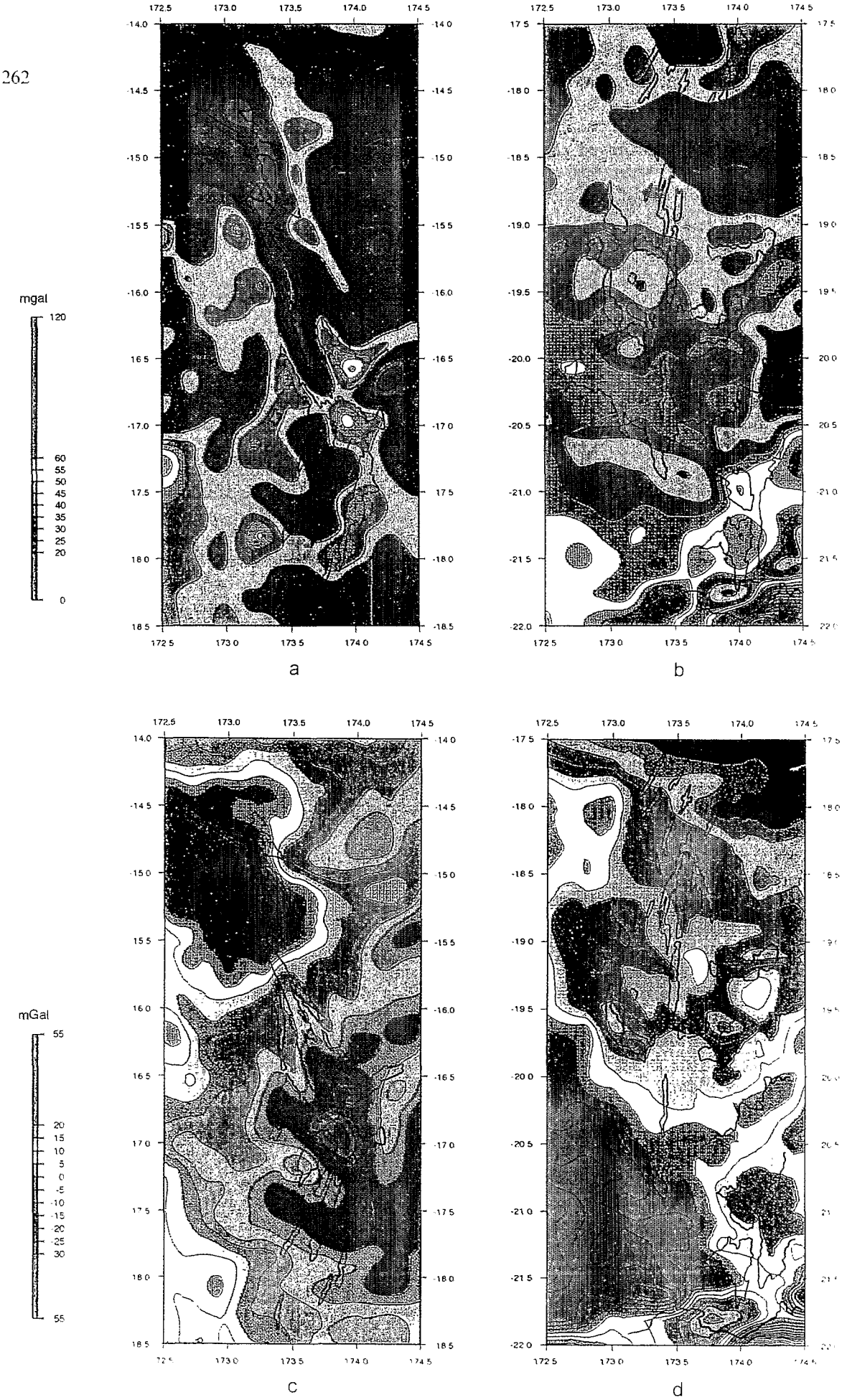
mgal
120
60
55
50
45
40
35
30
25
20
0
172.5
173.0
173.5
174.0
174.5
-14.0
-14.5
-15.0
-15.5
-16.0
-16.5
-17.0
-17.5
-18.0
-18.5
a
b
mGal
55
20
15
10
5
0
-5
-10
-15
-20
-25
-30
-55
c
d

data (Gràcia *et al.*, 1994) suggest near steady-state magmatism along axis. The off-axis topography is in general smooth and is only disturbed by the seamount chains that concentrate on the flanks of CSR7, the most magmatically robust segment.

The gravity structure beneath the CSR also shows strong differences between the northern and southern parts of the CSR. The N160° and N15° segments ("cold" spreading centers) have strong variations in the MBA, ranging from –55 to –10 mGal. The "bull's-eye"-shaped gravity lows observed in the 16°50′ S triple junction and in the middle of segments CSR2 and CSR3 are similar to the anomalies found between 27°50′ N and 30°40′ N in the Mid-Atlantic Ridge (Lin *et al.*, 1990; Rommevaux *et al.*, 1994) and also between 31° S and 34° S along the southern Atlantic (Kuo and Forsyth, 1988; Neumann and Forsyth, 1993). As suggested by Lin and Phipps-Morgan (1992) for slow spreading ridges, these negative anomalies are interpreted as mantle upwellings that result in a thickened crust.

The axis of the N–S segment ("hot" type) shows small-amplitude MBA variations (from –10 to 10 mGal), similar to the low gravity gradients observed along the East Pacific Rise at 9° N–13° N by Madsen *et al.* (1990). This can be interpreted as sheet-like accretion, a constant crustal thickness (Lin and Phipps-Morgan, 1992) and isostatic compensation of the axial topographic high (Madsen *et al.*, 1990).

Both morphologic and gravity features suggest two very different behaviours of magmatism: homogeneous and near steady-state magmatism along the N–S segment and heterogeneous and nonsteady-state magmatism along the N15° and N160° segments. Lava petrology supports this assumption (Table Ib). The lavas are predominantly N-MORB on the "hot" N–S segment. Along the N15° segment three magmatic sources coexist: N-MORB, BABB (transitional E-MORB with Nb anomaly) and OIB lavas. Along the N160° segments, the three sources still coexist, but the influence of the BABB source increases (Eissen *et al.*, 1994).

← Fig. 11. Left: Downgraded Free-Air (a) and Mantle Bouguer (c) Anomaly maps of the northern part of the Central Spreading Ridge (CSR). Right: Free-Air (b) and Mantle Bouguer (d) Anomaly maps of the southern part of the CSR. The original data of (a) and (c) (Figure 10) has been downgraded to be compared with the southern part of the CSR, where the gravity coverage is much more sparse. Superimposed, bold lines correspond to bathymetric contours to indicate the position of the main structural features.

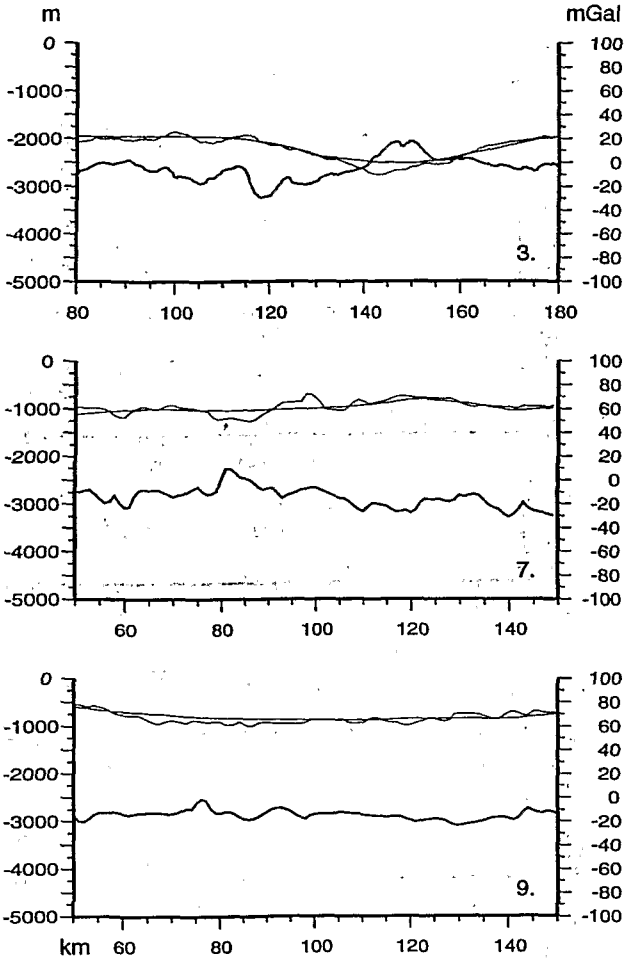


Fig. 12. Mantle Bouguer Anomalies computed along three ship profiles by removing at each data point the effect of the model from the Free-Air Anomaly, and compared to Mantle Bouguer Anomalies re-sampled from the merged satellite-marine data grid. Wavelengths longer than 50 km fit adequately. The corresponding bathymetric profiles are also displayed (*bold lines*). *See Figure 5 for profiles* location.

### 5.2. Unequivocal relationship between morphologic and gravity variability and spreading rate?

Chen and Morgan (1990a,b) presented a mechanical model to explain variations in axial topography and gravity with spreading rate. Their model is based on a layered rheology of the oceanic crust, with an upper brittle layer underlain by a ductile zone. The rheology is determined by the crustal thickness and the thermal structure of the lithosphere, and can result in the existence of a decoupling zone under the ridge axis (ductile lower crust). If the decoupling region is small or non-existent, as is the case for slow spreading ridges, then

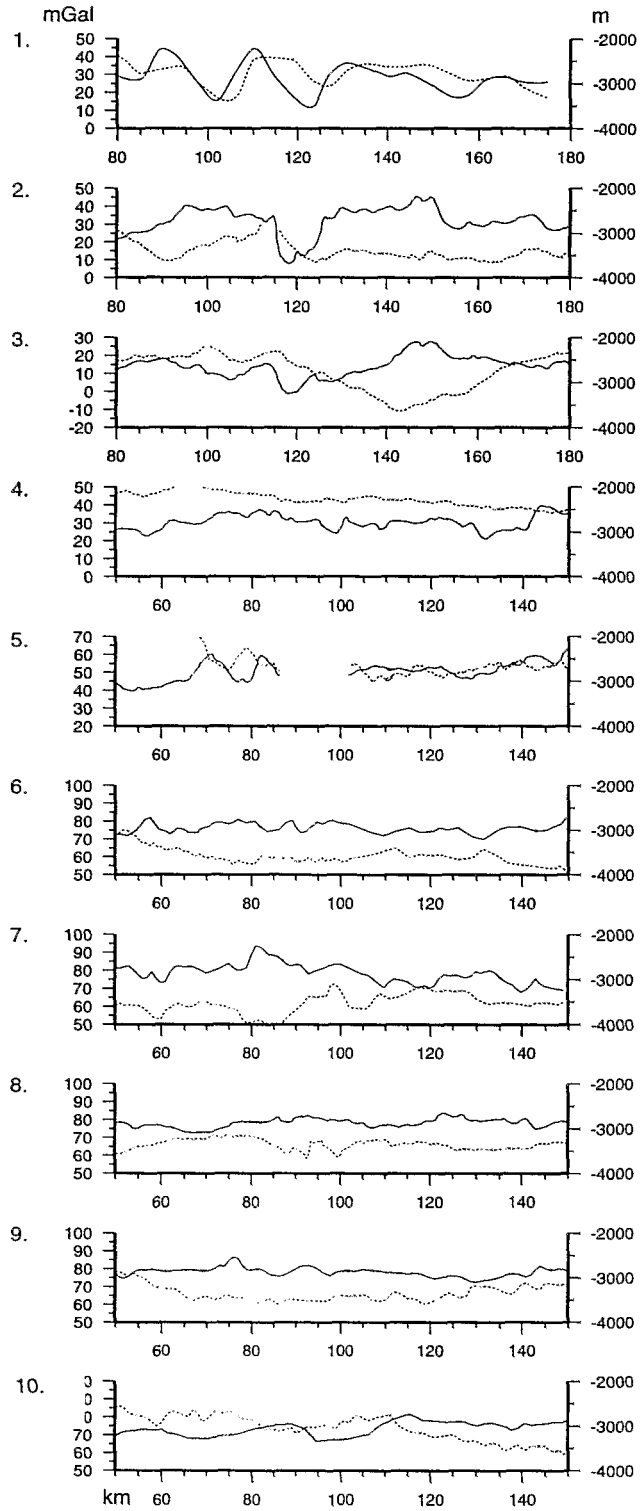


Fig. 13. Series of profiles representing bathymetry (continuous lines) and computed Mantle Bouguer Anomalies (dashed lines) along the Central Spreading Ridge. See Figure 5 for profiles location.

a rift valley is produced as a result of a necking process If the decoupling region is large, as it is suggested for the fast spreading ridges, a rise crest high is formed The critical spreading rate for the formation of a rift valley or a ridge morphology suggested by both topographic and gravity data is around 70 mm/yr.

A more evolved model is presented by Neumann and Forsyth (1993). They present a 3-D thermal model modified from that of Chen and Morgan (1990b) that includes passive mantle flow, hydrothermal circulation, plate boundary geometry and variable crustal thickness. The dynamic and isostatic loads produced by this model, applied to a moving, thickening plate, produce a median valley with relief and morphology controlled by the thickness of crust, spreading rate and mantle temperature.

The bathymetric, gravity and magmatic variations observed along-axis can be related to changes in spreading rate and crustal thickness (Phipps Morgan *et al.*, 1987; Chen and Morgan, 1990b; Neumann and Forsyth, 1993). With a critical spreading rate of 70 mm/yr, the changes in the observed morphologies along the CSR may, in part, be due to the decrease in spreading rate from 83 mm/yr to 50 mm/yr (south and north, respectively). However this progressive change in the spreading rate does not seem to be accompanied by important changes in the seismically-derived crustal thickness (Kisimoto *et al.*, 1994). Spreading rate and crustal thickness can only explain part of the variations in axial morphology and gravity observed. It is necessary to consider an additional explanation for the variability involving differences in the thermal regimes between the northern and southern segments of the CSR. This alternative hypothesis is tested by using a nonsteady-state thermal model, which allows us to take into account a variable heat supply beneath the axis.

### 5.3. Non steady-state thermal model for the Central Spreading Ridge

In this model (Tisseau and Tonnerre, 1995), the accretion is viewed as the superposition of two processes, spreading with creation of new oceanic crust and successive thermal inputs associated with magmatotectonic cycles.

To simulate the spreading a new two dimensional zone of crust and mantle is accreted at the ridge axis, at regular time intervals (Figure 14). Its width is 1 km and the spreading interval (dt) depends on the spreading rate value. At each time step (dt), new axial material is instantaneously emplaced, and its temperature profile ($T_{axis}$) is that of the neighboring zone.

TABLE I
Synthesis of the main results achieved after bathymetric and gravimetric analysis. Petrologic data are from Eissen *et al.* (1994).

a) Two crustal domains are distinguished on the North Fiji Basin

| Domain | Age (Ma) | Morphology | Gravity (MBA)[a] | Petrology |
|---|---|---|---|---|
| Old | 12 to 3.5 | uniform (3000 m) | strong positive anomalies (20 to 55 mGal) | BABB[b] (OIB)[c] |
| Young | 3.5 to 0 | irregular (2000–4000 m) | variable (15 to –55 mGal) | N-MORB[d] BABB (OIB) |

b) Two different types of spreading center are distinguished along the young domain or Central Spreading Ridge

| CSR | Morphology | | Magmatism | | MBA | Petrology |
|---|---|---|---|---|---|---|
| | off-axis | axis | off-axis | axis | | |
| Cold | rough | graben (N160°) and dome with graben (N15°) | absent | non permanent | strong variations (–55 to –10 mGal) | BABB N-MORB (OIB) |
| Hot | smooth | dome with ASC[e] (N-S) | present | permanent | weak variations (–10 to 10 mGal) | N-MORB (OIB) |

[a] Mantle Bouguer Anomaly.
[b] Back-Arc Basin Basalt.
[c] Ocean Island Basalt.
[d] Normal Mid-Ocean Ridge Basalt.
[e] Axial Summit Caldera.

Superimposed on spreading are magmato-tectonic cycles that are simulated as thermal inputs (temperature $T_{hs}$) occurring periodically in a 10 km-wide axial conduit, that extends vertically from 4 km below the seafloor to the bottom of the modelled box (Figure 14). Hot material rises very fast towards the surface (Dick, 1989), and thermal upwelling is modelled to be instantaneous. The periodicity of thermal upwelling events is assumed to be equal to the duration of a magmato-tectonic cycle. Time evolution is a succession of cycles of reheating followed by cooling. Temperature and melt fraction distributions are computed numerically step by step, both in space and time. The equations and numerical technique are detailed in the appendix.

We discuss below the modelling results corresponding to two hypothesis proposed for the CSR. To simulate the "cold" northern segment a half-spreading rate of 50 mm/yr is assumed, corresponding to that calculated at 17° S. A cycle of 200,000 yr reflects the periodicity of topographic lows and highs observed off-axis of the N160° and N15° segments. For the "hot" segments, a spreading rate of 83 mm/yr (calculated at 20°30′ S) is used, and a 120,000 yr cycle is considered, which corresponds to the periodicity of the off-axis topography along the N–S segment (see section 3.3).

### 5.4. Ridge thermal structure and partial melting

The results of the two CSR cases modelled are presented in Figures 15 and 16. In these figures we can see the temporal evolution and geometry of the thermal structure and the melting rate for the axial zone of the ridge.

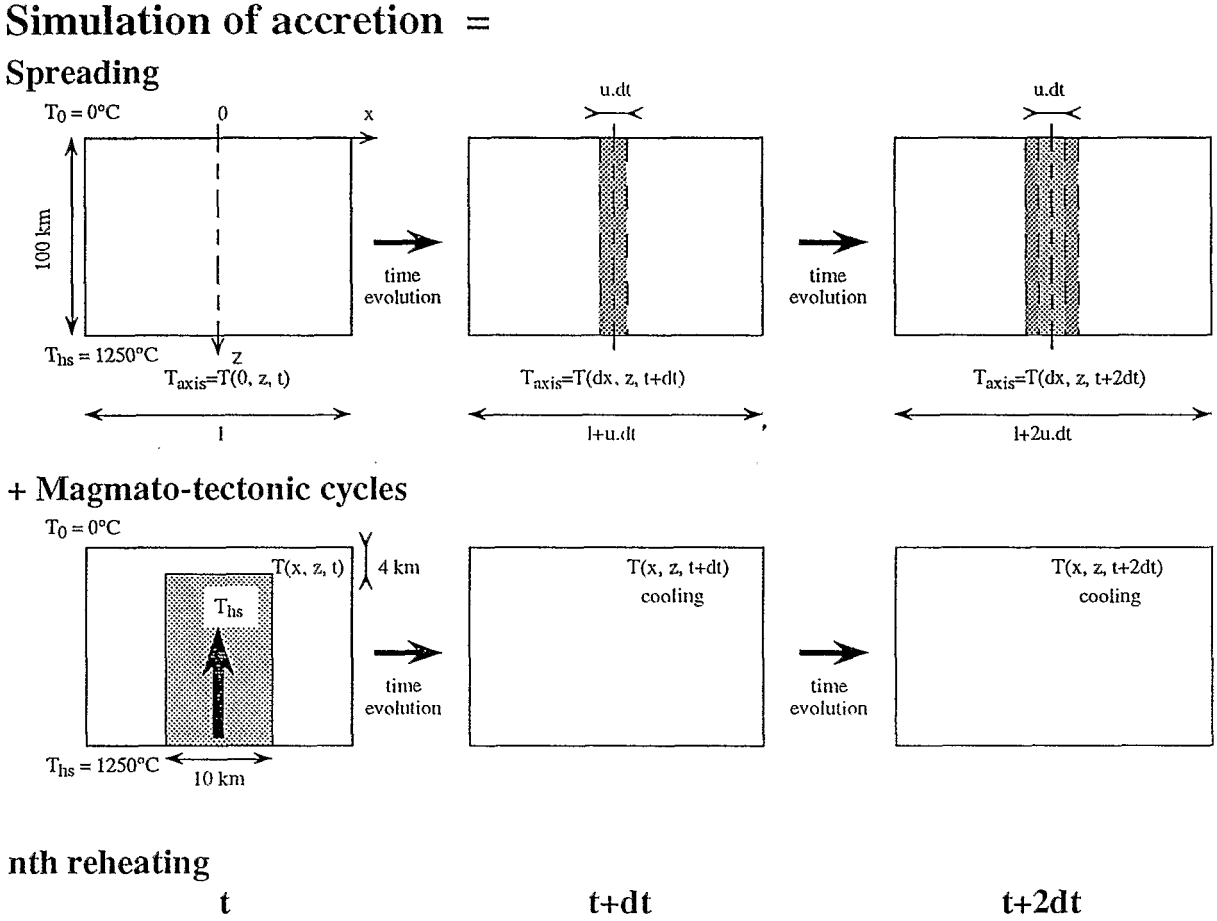


Fig. 14. Sketch of the thermal model used in this paper (modified from Tisseau and Tonnerre, 1995). The accretion is viewed as the superposition of the spreading (upper part) and magmato-tectonic cycles (lower part). 0: axis; $x$: across axis distance; z: depth; $t$: time; $u$: full spreading rate; $T$: temperature; $l$: full $x$-dimension of the computed box at $t$; $T_0$ and $T_{hs}$ upper and lower boundary temperatures respectively; $T_{axis}$: temperature at the axis and in the new created zone.

The results for the model of the northern part of the CSR (Figure 15) show progressive cooling in 40,000 year intervals. After the whole 200,000 yr cycle the isotherms are much more separated and deeper at the axial zone. This can be translated into thermal subsidence and the existence of a brittle, cold and thick lithosphere that fails by brittle necking resulting in the formation and development of an axial rift valley. In addition a strong deepening of the partial melting zone is seen, suggesting temporal variability in the magmatic regime. This corresponds well with the axial morphology observed on the N160° and N15° axes, and with the observed MBA structure.

The model results for the southern CSR (Figure 16) shows that, at the end of 120,000 yr cooling cycle, the isotherms remain grouped close to the surface at the ridge axis. The partial melting zone is still shallow and the magma budget is higher and more uniform in time than in the previous case. This thermal structure results in a thin, hot lithosphere with a lower ductile crust that acts as a decoupling zone. This situation is consistent with a fast East Pacific Rise type spreading center, resulting in a uniform topographic high, as observed along the N–S segment. In addition, this thermal structure is consistent with off-axis volcanism, also present in the N–S segment.

Fig. 15. Thermal modelling results for the northern part of the Central Spreading Ridge. A cycle of 200,000 yr and spreading rate $u = 50$ mm/yr are adopted. The model domain is 100 km wide and 50 km deep centered at the ridge axis. On the left side of each plot the temperature structure is shown, ranging from 0° to 1200 °C, in 100 °C contours. The right side corresponds to the melt fraction, ranging from 0% (white) to 22% (black).

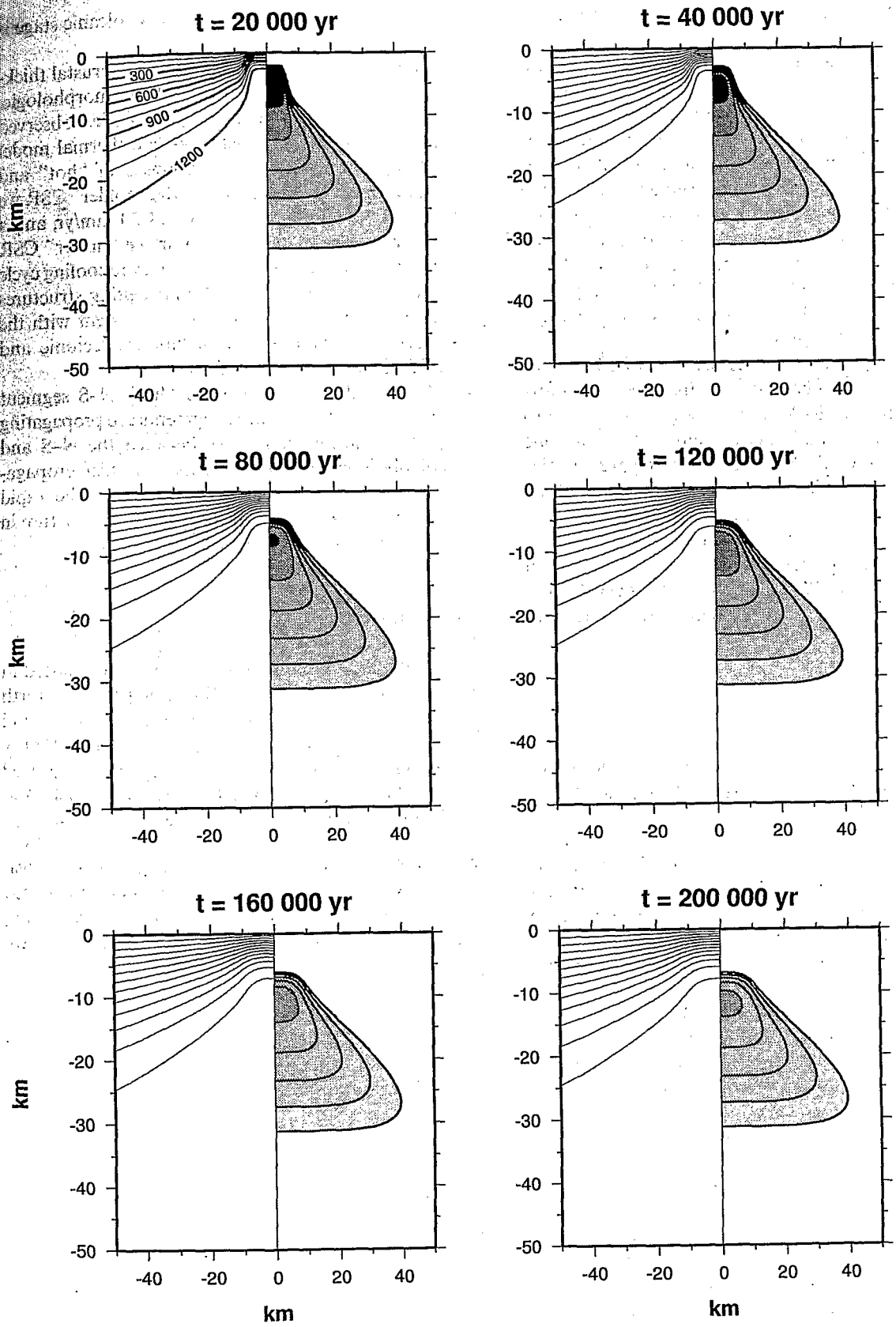
t = 20 000 yr
t = 40 000 yr
t = 80 000 yr
t = 120 000 yr
t = 160 000 yr
t = 200 000 yr
300
600
900
1200
km
0
-10
-20
-30
-40
-50
-40
-20
0
20
40

### 5.5. Heat propagation along the N–S segment

The boundaries between the "hot" N–S segment and its "cold" bounding segments are the 18°10′ S and 20°30′ S propagating rifts. Heat propagation along the N–S segment at the expense of the adjacent and colder failing segments may explain the rapid spatial changes in the observed morphology and structure between the segments. The hot segment is growing at the expense of the adjacent colder segments, as indicated by the direction of propagation of the segment boundaries (Macdonald *et al.*, 1992). At the CSR, the heat propagation southwards and northwards of the N–S segment started at least 1 Ma ago.

This kind of propagation has been proposed in other ridge environments. The dramatic change in axial morphology in the Pacific-Antarctic Ridge may be due to a propagation of "hot" asthenosphere from a zone north of the Udintsev Fracture Zone towards a relatively "colder" province to the south (Géli *et al.*, 1994). Another example is the Reykjanes Ridge, where an important V-shape ridge morphology structure has been interpreted as indication of heat-propagation originated at the Iceland hot-spot towards the south (Laughton *et al.*, 1979; Searle and Laughton, 1981).

## 6. Conclusions

1. Two axial morphologies are observed along the CSR: Mid-Atlantic Ridge or slow spreading type for the N160° segment, where tectonic processes dominate, and East Pacific Rise or fast spreading type for the N–S segment, dominated by magmatic processes. By contrast, the spreading rates do not show end-member values but have intermediate values decreasing northwards from 83 to 50 mm/yr. This variation in axial morphology cannot only be interpreted as differences in spreading rate, but also in thermal regime between the segments.
2. Deep crustal structure is inferred from the gravity (Mantle Bouguer Anomalies) analysis. Two domains (old and young) are proposed in the North Fiji Basin. For the young domain a distinction between a "cold" and a "hot" spreading type is proposed. The "cold" spreading center corresponds to the northern part of the CSR (comprising the N160° and N15° segments), and is characterized by weak magmatism related to a low thermal budget similar to other slow spreading ridges. The "hot" spreading ridge corresponds to the southern part of the CSR (N–S segment) where a high thermal supply related to a more vigorous volcanic stage is suggested.
3. Differences in the spreading rate and crustal thickness can only explain a part of the morphologic, gravimetric and magmatic variabilities observed along the CSR. A nonsteady-state thermal model is proposed to test our hypothesis of "hot" and "cold" spreading centers. For the "colder" CSR we have adopted a spreading rate of 50 mm/yr, and a cooling cycle of 200,000 yr. For the "hotter" CSR the spreading rate is 83 mm/yr and the cooling cycle is 120,000 yr. The thermal and melting structures resulting from the models are consistent with the observed variations in morphology, tectonic and volcanic style along the CSR.
4. The boundaries between the "hot" N–S segment and the "cold" bounding segments are propagating rifts. A thermal boundary between the N–S and neighbouring colder segments, and heat propagation along the N–S axis may explain the rapid changes in the axial morphologies and structure in depth between the segments.

## Acknowledgments

We would like to thank all the people who assisted in the collection of the Central Spreading Ridge (North Fiji Basin) data, including the captains, crews and scientific parties of the French-Japanese STARMER project (1987–1991). M. Tanahashi gave us a reduced grid of the original bathymetric data. J. Escartín and H. Ondréas gave us useful comments of a first draft of this paper. P. Halbach, J. Madsen and M.C. Sinha for careful review and suggestions to improve the clarity of the manuscript and figures. Many of the figures of this paper were made using the GMT graphics package of P. Wessel and W. Smith. E. Gràcia

## Appendix: Thermal Modelling

(modified from Tisseau and Tonnerre, 1995)

*Equations*

The basic equation in our thermal model is the two-dimensional heat equation for a nonsteady-state regime, taking into account horizontal and vertical

Fig. 16. Thermal modelling results for the southern part of the Central Spreading Ridge. A cycle of 120,000 yr and spreading rate $u=83$ mm/yr are adopted. See Figure 15 for explanations

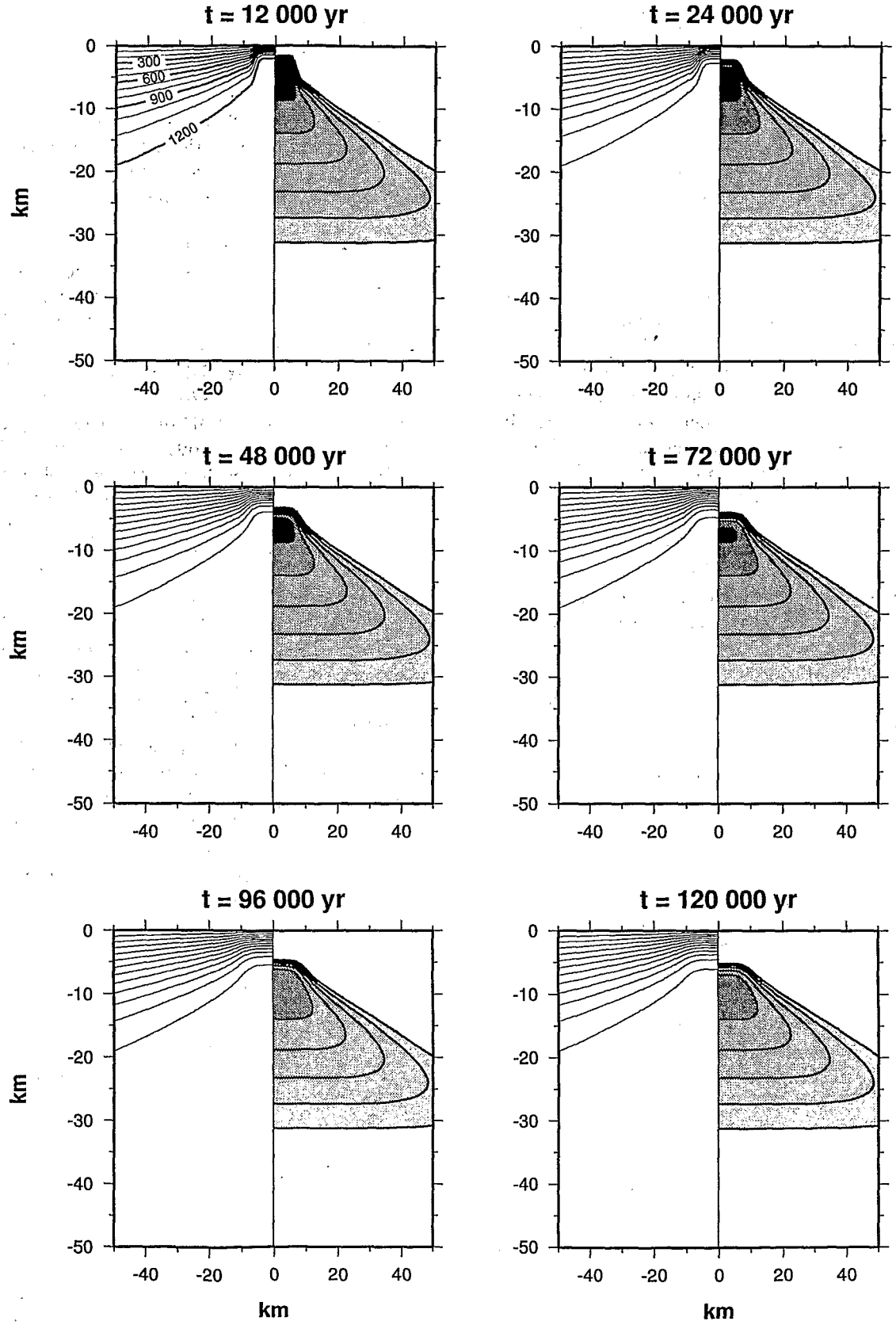
t = 12 000 yr
t = 24 000 yr
t = 48 000 yr
t = 72 000 yr
t = 96 000 yr
t = 120 000 yr
300
600
900
1200
0
-10
-20
-30
-40
-50
-40
-20
0
20
40
km

conductive heat transfer and heat loss due to partial melting:

$$\frac{\partial}{\partial t}T(x,z,t)=K\left(\frac{\partial^2}{\partial x^2}+\frac{\partial^2}{\partial z^2}\right)T(x,z,t)-\left(\frac{L}{c}\right)\frac{\partial}{\partial t}M(x,z,t) \quad (1)$$

where:

$T(x, z, t)$ = temperature as a function of the across-axis distance $x$, depth $z$, and time $t$;

$K$ = thermal diffusivity;

$c$ = specific heat;

$L$ = latent heat of melting;

$M(x, z, t)$ = melt fraction depending on $T(x, z, t)$.

The heat transfer associated with spreading, currently introduced as a convective term in the heat equation, is partly taken into account in our model via a succession of temperature reinitiations through time as outlined below. No additional heat contribution is introduced in equation (1) because the radiogenic heat production in the oceanic crust is too low. The thermal effect of hydrothermal circulation, often modelled as a heat loss at shallow depths, is not taken into account in this study. There is insufficient information at present to constrain the temporal evolution of hydrothermal circulation, however, it is clearly episodic such that a steady-state heat loss would be unrealistic. Moreover, the effect of hydrothermal circulation is probably limited to shallow levels and does not significantly affect the thermal state at greater depth.

The melt fraction $M(x, z, t)$ is expressed as a function of temperature and pressure, from McKenzie (1984):

$$M(x,z,t)=100\,\frac{T(x,z,t)-T_{sol0}-S_{sol}\cdot p(x,z,t)}{T_{liq0}-T_{sol0}-(S_{sol}-S_{liq})\cdot p(x,z,t)} \quad (2)$$

where:

$M(x, z, t)$ = melt fraction (in percent);

$T(x, z, t)$ = temperature as a function of the across-axis distance $x$, depth $z$, and time $t$;

$p(x, z, t)$ = pressure as a function of the across-axis distance $x$, depth $z$, and time $t$;

$T_{sol\,0}$ = solidus temperature at $z=0$;

$T_{liq\,0}$ = liquidus temperature at $z=0$;

$S_{sol}$ = slope of the solidus;

$S_{liq}$ = slope of the liquidus.

Parameter values used in the computation are listed in Table II.

For each computational step in time $\Delta t$ (see below), we first solve equation (1) assuming that no melting occurs, and obtain the distribution of the mantle potential temperature. For regions in which this potential temperature is above the solidus, temperatures are calculated again, taking into account the latent heat of melting. Finally, the melt fraction distribution is deduced from equation (2).

*Spatial and temporal discretization*

The solution of the differential equation (1) is obtained by the finite difference method. The numerical integration is based on alternating-direction implicit methods. For this study, the computational steps are as follows:

| | | |
|---|---|---|
| in space, | $\Delta x=\Delta z=500$ m | |
| in time, | $\Delta t=2000$ yr | for the N160° and N15° segments |
| | $\Delta t=1200$ yr | for the N–S segment |

The value of the spatial step $\Delta x$ has been chosen to have a reasonable number of computational nodes within both the new axial zone created by spreading (here 1 km wide, i.e., 3 nodes) and the axial thermal conduit (here 10 km wide, i.e., 21 nodes). The dimensions of the computational domain are 100 km in depth and 100 km in the $x$-direction at time $t=0$ when initial conditions are set. This last $x$-dimension (shown as l in Figure 14) increases with time as the result of spreading. A good convergence of the discrete solution in time needs a number of iterations of about 20 for such a grid, i.e., a time interval of 10 times $\Delta t$ between two successive temperature results.

*Boundary conditions*

The temperature is set to a constant both at the upper boundary (equal to $T_0$) and at the lower boundary (equal to $T_{hs}$, see Table II for numerical values). At lateral boundaries, the value of lateral heat flow is set to zero. In order to avoid edge effects in the zone of interest, these lateral boundaries are chosen sufficiently far away from this zone.

*Initial conditions and reinitiations at regular time steps*

At time $t=0$, the initial temperature distribution is calculated from the half-space model of lithospheric cooling (Davis and Lister, 1974).

At regular time steps, we reinitiate the temperature distribution in the axial domain, either in a new narrow zone created by the spreading, with each spreading time step $dt$ (Figure 14, upper part), or in the axial conduit at the start of each magmato-tectonic cycle (Fig. 14, lower part), or both.

The thermal evolution is computed through time for computational time steps $\Delta t$ given previously. We only use the temperature results obtained after 5 or 6 magmato-tectonic cycles, when the thermal regime is stabilized for 2 successive cycles.

TABLE II
Physical parameters

| Variable | Meaning | Value | Units |
|---|---|---|---|
| *Heat equation parameters* | | | |
| $\rho_m$ | density of mantle at 0 °C | 3.33 | |
| $\rho$ | density of mantle at temperature $T=\rho_m(1-\alpha T)$ | | |
| $\alpha$ | thermal expansion coefficient | $3.28\ 10^{-5}$ | $°C^{-1}$ |
| $k$ | thermal conductivity | 3.14 | $W\ m^{-1}\ °C^{-1}$ |
| $K$ | thermal diffusivity | $1.13\ 10^{-6}$ | $m^2\ s^{-1}$ |
| $c$ | specific heat $=k/\rho K$ | | |
| $L$ | latent heat of melting | 720 | $J\ kg^{-1}\ °C^{-1}$ |
| *Melting equation parameters* | | | |
| $T_{sol\,0}$ | solidus temperature at $z=0$ | 1115 | °C |
| $T_{liq\,0}$ | liquidus temperature at $z=0$ | 1715 | °C |
| $S_{sol}$ | slope of the solidus | 120 | $°C\ GPa^{-1}$ |
| $S_{liq}$ | slope of the liquidus | −16 | $°C\ GPa^{-1}$ |
| *Boundary conditions* | | | |
| $T_0$ | upper boundary temperature | 0 | °C |
| $T_{hs}$ | lower boundary temperature | 1250 | °C |

## References


Anderson, R. N. and Noltimier, H. C., 1973, A Model for the Horst and Graben Structure of Mid-Ocean Ridge Crests Based on Spreading Velocities and Basalt Delivery to the Ocean Crust, *Geophys. J. R. Astron. Soc.* **34**, 137–149.

Atwater, T. and Mudie, J. D., 1973, Detailed Near-Bottom Geophysical Study of the Gorda Rise, *J. Geophys. Res.* **78**, 8665–8686.

Auzende, J. M., Eissen, J. P., Lafoy, Y., Gente, P. and Charlou, J. L., 1988a, Seafloor Spreading in the North Fiji Basin (Southwest Pacific), *Tectonophysics* **146**, 317–351.

Auzende, J. M., Lafoy, Y. and Marsset, B., 1988b, Recent Geodynamic Evolution of the North Fiji Basin (SW Pacific), *Geology* **16**, 925–929.

Auzende, J. M., Honza, E., Boespflug, X., Deo, S., Eissen, J. P., Hashimoto, J., Huchon, P., Ishibashi, J., Iwabuchi, Y., Jarvis, P., Joshima, M., Kisimoto, K., Kiuwahara, Y., Lafoy, Y., Matsumoto, T., Mazé, J. P., Mitsuzawa, K., Momma, H., Naganuma, T., Nojiri, Y., Ohta, S., Otsuka, K., Okuda, Y., Ondréas, H., Otsuki, A., Ruellan, E., Sibuet, M., Tanahashi, M., Tanaka, T. and Urabe, T., 1990, Active Spreading and Hydrothermalism in North Fiji Basin (SW Pacific). Results of Japanese-French Cruise Kaiyo 87, *Mar. Geophys. Res.* **12**, 269–283.

Auzende, J. M., Urabe, T., Bendel, V., Deplus, C., Eissen, J. P., Grimaud, D., Huchon, P., Ishibashi, J., Joshima, M., Lagabrielle, Y., Mével, C., Naka, J., Ruellan, E., Tanaka, T. and Tanahashi, M., 1991, In Situ Geological and Geochemical Study of an Active Hydrothermal Site on the North Fiji Basin Ridge, *Mar. Geol.* **98**, 259–269.

Auzende, J. M., Gràcia Mont, E., Bendel, V., Huchon, P., Lafoy, Y., Lagabrielle, Y., De Alteriis, G. and Tanahashi, M., 1994, A Possible Triple Junction at 14°50′ S on the North Fiji Basin Ridge (Southwest Pacific)?, *Mar. Geol.* **116**, 25–37.

Batiza, R. and Banko, D., 1983, Volcanic Development of Small Oceanic Central Volcanoes on the Flanks of the East Pacific Rise Inferred from Narrow-Beam Echosounder Surveys, *Mar. Geol.* **54**, 53–90.

Bendel, V., Fouquet, Y., Auzende, J. M., Lagabrielle, Y., Grimaud, D. and Urabe, T., 1993, The White Lady Hydrothermal Field, North Fiji Back-Arc Basin, Southwest Pacific, *Economic Geol.* **88**, 2237–2249.

Carbotte, S. M. and Macdonald, K. C., 1990, Causes of Variation in Fault-Facing Direction on the Ocean Floor, *Geology* **18**, 749–752.

Chen, Y. and Morgan, W. J., 1990a, Rift Valley/No Rift Valley Transition at Mid-Ocean Ridges, *J. Geophys. Res.* **95**, 17571–17581.

Chen, Y. and Morgan, W. J., 1990b, A Nonlinear Rheology Model for the Mid-Ocean Ridge Axis Topography, *J. Geophys. Res.* **95**, 17583–17604.

Davis, E. E. and Lister, C. R. B., 1974, Fundamentals of Ridge Crest Topography, *Earth Planet. Sci. Lett.* **21**, 405–413.

De Alteriis, G., Ruellan, E, Auzende, J. M., Ondréas, H., Bendel, V., Gràcia Mont, E., Huchon, P., Lagabrielle, Y. and Tanahashi, M., 1993, Propagating Rifts in the North Fiji Basin (Southwest Pacific), *Geology* **21**, 533–536.

Dick, H. J. B., 1989, Abissal Peridotites, Very Slow Spreading Ridges and Ocean Ridge Magmatism, in Saunders, A. D. and Norry, M. J. (eds.), *Magmatism in the Ocean Basins*, Geol. Soc. Sp. Publ. 71–105.

Eissen, J. P., Lefèvre, C., Maillet, P., Morvan, G. and Nohara, M., 1991, Petrology and Geochemistry of the Central North Fiji Basin Spreading Centre (Southwest Pacific) between 16° S and 22° S, *Mar. Geol.* **98**, 201–239.

Eissen, J. P., Nohara, M. and Cotten, J., 1994, North Fiji Basin Basalts and their Magma Sources: Part I. Incompatible Elements Constraints, *Mar. Geol.* **116**, 153–179.

Fox, P. J., Grindlay, N. R. and Macdonald, K. C., 1991, The Mid-Atlantic Ridge (31° S–34°30′ S): Temporal and Spatial Variations of Accretionary Processes, *Mar. Geophys. Res.* **13**, 1–20.

Géli, L., Ondréas, H., Olivet, J. L., Sahabi, M., Aslanian, D. and Gilg-Capar, L., 1994, Thermal Structure vs. Spreading Rate at Intermediate Spreading Rates: The Example of the Pacific-Antarctic Ridge between 55° S and 63° S, *EOS Trans. AGU* **7**, 330.

Gràcia, E., Ondréas, H., Bendel, V. and STARMER group, 1994, Multi-Scale Morphologic Variability of the North Fiji Basin Ridge (Southwest Pacific), *Mar. Geol.* **116**, 133–153.

Grindlay, N. R., Fox, P. J. and Vogt, P. R., 1992, Morphology and Tectonics of the Mid-Atlantic Ridge (25°–27°30′ S) from SeaBeam and Magnetic Data, *J. Geophys. Res.* **97**, 6983–7010.

Hey, R., Duennebier, F. K. and Morgan, W. J., 1980, Propagating Rifts on Mid-Ocean Ridges, *J. Geophys. Res.* **85**, 3647–3658.

Hsu, S. K., 1995, XCORR: A Cross-Over Technique to Adjust Track Data, *Comp. and Geosci.* **21**, 259–271.

Huchon, P., Gràcia, E., Ruellan, E., Joshima, M. and Auzende, J. M., 1994, Kinematics of Active Spreading in the Central North Fiji Basin (SW Pacific), *Mar. Geol.* **116**, 69–89.

Inoue, H., 1986, A Least-Square Smooth Fitting for Irregularly Spaced Data: Finite-Element Approach Using the Cubic B-Spline Basis, *Geophysics* **51**, 2051–2061.

Jarvis, P. and Kroenke, L., 1993, Structural Development of the Central North-Fiji Basin Triple Junction, *Geo-Mar. Lett.* **13**, 133–138.

Kappel, E. S. and Ryan, W. B. F., 1986, Volcanic Episodicity and a Nonsteady-State Rift Valley Along the Northeast Pacific Spreading Centers: Evidence from Sea-Marc I, *J. Geophys. Res.* **91**, 13925–13940.

Kisimoto, K., Tanahashi, M. and Auzende, J. M., 1994, Crustal Structure Variation Along the Central Rift-Ridge Axis in the North-Fiji Basin: Implications from Seismic Reflection and Refraction Data, *Mar. Geol.* **116**, 101–111.

Kroenke, L. W., Eade, J. V. and Scientific Party, 1990, Overview and Principal Results of the Second Leg of the First Joint CCOP/SOPAC-Tripartite Cruise of the R/V Kana-Keoki: North Fiji Basin Survey (KK820316 Leg 3), in Kroenke, L. W. and Eade, J. V. (eds.), *Basin Formation, Ridge Crest Processes and Metallogenesis in the North Fiji Basin,* Circum Pacific Council for Energy and Mineral Resources, Earth Science Series **12**, 1–13.

Kuo, B. and Forsyth, D., 1988, Gravity Anomalies of the Ridge-Transform System in the South Atlantic Between 31° and 34.5° S: Upwelling Centers and Variations in Crustal Thickness, *Mar. Geophys. Res.* **10**, 205–232.

Lachenbruch, A., 1973, A Simple Mechanical Model for Oceanic Spreading Centers, *J. Geophys. Res.* **78**, 3395–3417.

Lafoy, Y., Auzende, J. M., Ruellan, E., Huchon, P. and Honza, E., 1990, The 16°40′ S Triple Junction in the North Fiji Basin (SW Pacific), *Mar. Geophys. Res.* **12**, 285–296.

Lagabrielle, Y., Ruellan, E., Tanahashi, M., Pelletier, B., Bourgois, J., Buffet, G., de Alteriis, G., Dyment, J., Goslin, J., Gràcia, E., Iwabuchi, I., Jarvis, P., Joshima, M., Karpoff, A. M., Matsumoto, T., Ondréas, H. and Sardou, O., 1994, Active Spreading Along the South Pandora Ridge in the North Fiji Basin (SW Pacific): First Results of the NOFI Cruise (French-Japanese New Starmer Program), *EOS, Trans. AGU* **75**, 673.

Laughton, A. S., Searle, R. C. and Roberts, D. G., 1979, The Reykjanes Ridge Crest and the Transition between its Rifted and Non-Rifted Regions, *Tectonophysics* **55**, 173–177.

Lin, J. and Phipps-Morgan, J., 1992, The Spreading Rate Dependence of Three-Dimensional Mid-Ocean Ridge Gravity Structure, *Geophys. Res. Lett.* **19**, 13–16.

Lin, J., Purdy, G. M., Schouten, H., Sempéré, J. C. and Zervas, C., 1990, Evidence from Gravity Data for Focused Magmatic Accretion Along the Mid-Atlantic Ridge, *Nature* **344**, 627–632.

Macdonald, K. C., 1982, Mid-Ocean Ridges: Fine Scale Tectonic, Volcanic and Hydrothermal Processes within the Plate Boundary Zone, *Ann. Rev. Earth Planet. Sci.* **10**, 155–190.

Macdonald, K. C., 1986, The Crest of the Mid-Atlantic Ridge: Models for Crustal Generation and Tectonics, in Vogt, P. R. and Tucholke, B. E. (eds.), *The Geology of North-America,* **vol. M,** *The Western North Atlantic Region*, Geological Society of America, Boulder, CO., 51–68.

Macdonald, K. C. and Fox, P. J., 1983, Overlapping Spreading Centers: A New Kind of Accretion Geometry on the East Pacific Rise, *J. Geophys. Res.* **88**, 9393–9406.

Macdonald, K. C. and Fox, P. J., 1988, The Axial Summit Graben and Cross-Sectional Shape of the East Pacific Rise as Indicators of Axial Magma Chambers and Recent Volcanic Eruptions, *Earth Planet. Sci. Lett.* **88**, 119–131.

Macdonald, K. C., Scheirer, D. S. and Carbotte, S. M., 1991, Mid-Ocean Ridges: Discontinuities, Segments and Giant Cracks, *Science* **253**, 986–994.

Macdonald, K. C., Fox, P. J., Miller, S., Carbotte, S., Edwards, M. H., Eisen, M., Fornari, D. J., Perram, L., Pockalny, R., Scheirer, D., Tighe, S., Weiland, C. and Wilson, D., 1992, The East Pacific Rise and its Flanks 8°–18° N: History of Segmentation, Propagation and Spreading Direction based on SeaMarc II and SeaBeam studies, *Mar. Geophys. Res.* **14**, 299–344.

Madsen, J. A., Detrick, R. S., Mutter, J. C., Buhl, P. and Orcutt, J. A., 1990, A Two- and Three-Dimensional Analysis of Gravity Anomalies Associated with the East Pacific Rise at 9° N and 13° N, *J. Geophys. Res.* **95**, 4967–4987.

Malinverno, A., 1993, Transition between a Valley and a High at the Axis of Mid-Ocean Ridges, *Geology* **21**, 639–642.

Marks, K. M. and Stock, J. M., 1994, Variations in Ridge Morphology and Depth Age Relationships on the Pacific-Antarctic Ridge, *J. Geophys. Res.* **99**, 531–541.

Martinez, F., Naar, D. F., Reed IV, T. B. and Hey, R. N., 1991, Three-Dimensional SeaMarc II, Gravity, and Magnetics Study of Large-Offset Rift Propagation at the Pito Rift, Easter Microplate, *Mar. Geophys. Res.* **13** (4), 255–287.

McKenzie, D., 1984, The Generation and Compactation of Partially Molten Rock, *J. Petro.* **25**, 713–765.

Menard, H. W., 1967, Seafloor Spreading, Topography and the Second Layer, *Science* **157**, 923–924.

Neumann, G. and Forsyth, D., 1993, The Paradox of the Axial Profile: Isostatic Compensation Along the Axis of the Mid-Atlantic Ridge?, *J. Geophys. Res.* **98**, 17891–17910.

Neumann, G., Forsyth, D. and Sandwell, D., 1993, Comparison of Marine Gravity from Shipboard and High-Density Satellite Altimetry Along the Mid-Atlantic Ridge, 30.5° S – 35.5° S, *Geophys. Res. Lett.* **20**, 1639–1642.

NOAA/NGDC, 1992, GEODAS Marine Geophysical Data, 2 CD-ROM.

Palmer, J., Sempéré, J. C., Christie, D. M. and Phipps Morgan, J., 1993, Morphology and Tectonics of the Australian-Antarctic Discordance between 123° E and 128° E, *Mar. Geophys. Res.* **15**, 121–152.

Parker, R., 1972, The Rapid Calculation of Potential Anomalies, *Geophys. J. R. Astr. Soc.* **31**, 447–455.

Parson, L. M., Hawkins, J. W. and Allan, J. F., Eds., 1992, *Proceedings of the Ocean Drilling Program*, Scientific Results **135**, Ocean Drilling Program, College Station, TX.

Pelletier, B., Lafoy, Y. and Missegue, F., 1993, Morphostructure and Magnetic Fabric of the Northwestern North Fiji Basin, *Geophys. Res. Lett.* **20**, 1151–1154.

Phipps Morgan, J., Parmentier, E. M. and Lin, J., 1987, Mechanisms for the Origin of Mid-Ocean Ridge Axial Topography: Implications for the Thermal and Mechanical Structure of Accreting Plate Boundaries, *J. Geophys. Res.* **92**, 12823–12836.

Prince, R. and Forsyth, D., 1988, Horizontal Extent of Anomalously thin Crust Near the Vema Fracture Zone from the Three-Dimen-

sional Analysis of Gravity Anomalies, *J. Geophys. Res.* **93**, 8051–8063.

Purdy, G. M., Sempéré, J. C., Schouten, H., Dubois, D. L. and Goldsmith, R., 1990, Bathymetry of the Mid-Atlantic Ridge, 24°–31° N: A Map Series, *Mar. Geophys. Res.* **12**, 247–252.

Rommevaux, C., Deplus, C., Patriat, P. and Sempéré, J. C., 1994, Three-Dimensional Gravity Study of the Mid-Atlantic Ridge: Evolution of the Segmentation between 28° and 29° N during the Last 10 m.y., *J. Geophys. Res.* **99**, 3015–3029.

Ruellan, E., Huchon, P., Auzende, J. M. and Gràcia, E., 1994, Propagating Rifts and Overlapping Spreading Centers in the North Fiji Basin, *Mar. Geol.* **116**, 37–57.

Sandwell, D. and Smith, W., 1992, Global Marine Gravity from ERS–1 Geosat and Seasat Reveals New Tectonic Fabric, *EOS Trans., AGU* **73**, 133.

Schouten H., Klitgord, K. and Whitehead, J., 1985, Segmentation of Mid-Ocean Ridges, *Nature* **317**, 225–229.

Searle, R. C. and Laughton, A. S., 1981, Fine Scale Sonar Study of Tectonics and Volcanism on the Reykjanes Ridge, *Oceanol. Acta* **4**, 5–18.

Shen, Y., Forsyth, D. W., Scheirer, D. and Macdonald, K. C., 1993, Two forms of Volcanism: Implications for Mantle Flow and Off-Axis Crustal Production on the West Flank of the Southern East Pacific Rise, *J. Geophys. Res.* **98**, 17875–17889.

Sleep, N., 1969, Sensivity of Heat-Flow and Gravity to the Mechanism of Seafloor Spreading, *J. Geophys. Res.* **74**, 542–549.

Tanahashi, M., Kisimoto, K., Joshima, M., Jarvis, P., Iwabuchi, Y., Ruellan, E. and Auzende, J. M., 1994, 800 km Long N–S Spreading System of the North Fiji Basin, *Mar. Geol.* **116**, 10–24.

Tapponnier, P. and Francheteau, J., 1978, Necking of the Lithosphere and the Mechanics of Slowly Accreting Plate Boundaries, *J. Geophys. Res.* **83**, 3955–3970.

Taylor, B., Goodliffe, A., Martínez, F. and Hey, R., 1995, Continental Rifting and Initial Sea-Floor Spreading in the Wodlark Basin, *Nature* **374**, 534–537.

Tisseau, C. and Tonnerre, T., 1995, Non Steady-State Thermal Model of Spreading Ridges: Implications for Melt Generation and Mantle Outcrops, in Vissers, R. L. M. and Nicolas, A. (eds.), *Mantle and Lower Crust Exposed in Oceanic Ridges and in Ophiolites,* Kluwer Academic Pub., Neth., 181–214.

Whitehead, J. Jr., Dick, H, and Schouten, H., 1984, A Mechanism for Magmatic Accretion under Spreading Centers, *Nature* **312**, 146–148.

Marine Geophysical Researches / *Volume 18 Nos. 2–4 June 1996*

Special Issue

# Seafloor Mapping in the West, Southwest and South Pacific: Results and Applications



*Guest Editors*
JEAN-MARIE AUZENDE and JEAN-YVES COLLOT